

Coincidence laser spectroscopy (CLS) for the detection of ions in ICP-MS (ICP-MS-CLS). A feasibility study†

Barry L. Sharp,*^a Phillip S. Goodall,^b Ljubinko M. Ignjatovic^c and Huaguo Teng^d

Received 15th May 2007, Accepted 11th July 2007

First published as an Advance Article on the web 22nd August 2007

DOI: 10.1039/b707394c

This paper reports a theoretical study of the feasibility of using laser-excited ionic fluorescence in time correlation with ion counting, termed coincidence laser spectroscopy (CLS), for improved specificity in the detection of ions in ICP-MS. The technique is here named ICP-MS-CLS. A number of factors are considered including: the preferred instrumental configuration, simulation of the performance of the optical detector and correlation step in reducing background, the spectroscopy of the selected isotopes, $^{10}\text{Be}^+$, $^{55}\text{Fe}^+$, $^{63}\text{Ni}^+$, $^{90}\text{Sr}^+$, $^{99}\text{Tc}^+$, $^{147}\text{Pm}^+$, $^{238}\text{U}^+$, $^{238}\text{Pu}^+$ and $^{241}\text{Am}^+$, which might be appropriate candidates for ICP-MS-CLS detection, the laser power required to attain saturation, the effects of ion energy and energy spread on pumping efficiency, the optical abundance sensitivity for adjacent isotopes of the same element, and the detection limits obtainable under a variety of scenarios. The ICP is established as an ideal ion source for elemental mass spectrometry, but as shown here, the ion energy spread produced is too large for optimum optical pumping because the ions are Doppler shifted to an extent that not all of them would be excited efficiently by a narrow-line laser source. This necessitates the inclusion of an ion cooler into the instrumental configuration so that ions may be brought into resonance with the laser with 100% efficiency. The calculations show that for ions with simple spectra, such as $^{90}\text{Sr}^+$ which can be repetitively pumped by the laser to produce a photon burst, ICP-MS-CLS can reduce the effect of very high backgrounds, 10^6 cps on mass and 10^{10} cps at adjacent mass, to low levels and improve detection limits by 2–3 orders of magnitude compared with the normal technique. Optical abundances of 10^{-5} – 10^{-9} are achievable which, combined with the mass abundance sensitivity of 10^{-5} , yields overall abundance sensitivities of 10^{-10} – 10^{-14} . This is of the same order as techniques such as accelerator mass spectrometry (AMS) or resonance ionisation mass spectrometry (RIMS). The technique is much less efficient for ions that undergo optical trapping and emit only one photon when pumped and/or exhibit hyperfine structure which distributes the oscillator strength over several hyperfine components. These factors significantly degrade performance and indicate a requirement for further refinement in terms of using two-colour excitation, or quenching of meta-stable levels, to enable the recycling of ions for further pumping.

Introduction

An evolving area of interest in ICP-MS is the determination of radionuclides that have traditionally been measured using various radiometric counting techniques, *e.g.*, α -spectrometry, liquid scintillation counting and γ -spectrometry. It is often not appreciated that the major challenge in classical analytical radiochemistry is one of separation of the analyte from both the matrix and concomitant analytes. The standard radiochemical approaches rely heavily upon classical inorganic

separation techniques, and the development of a highly specific and sensitive instrumental approach would be a revolutionary event in radioanalytical chemistry. The advantages of utilizing ICP-MS for radionuclide determinations may include: improved limits of detection, simple sample preparation when compared to radiometric techniques, reduced facilities required for that sample preparation, faster turnaround times, improved throughputs *etc.*

There are, in general, two aims of a radionuclide environmental or biomedical monitoring program. Firstly, to assess accurately the radiological dose to an individual, a critical group or the biosphere in general and secondly, in support of non-proliferation measures. When considering the application of ICP-MS to a radiochemical analysis, the information content of that analysis cannot be degraded with respect to a more conventional radiochemical procedure. For example, in dosimetry, all isotopes of an element that might give rise to a specific and significant dose must be included in the determination. The benchmark in the nuclear industry for an

^a Department of Chemistry, Loughborough University, Loughborough, Leicestershire, UK LE11 3TU. E-mail: b.l.sharp@lboro.ac.uk

^b Nexia Solutions, Sellafield, Seascale, Cumbria, UK CA20 1PG

^c Institute of Physics, Beograd, Yugoslavia

^d SERCO Ltd., Manchester, UK

† Electronic supplementary information (ESI) available: Description of the programme "CO-IN" which models the CLS detector, calculation of the hyperfine splitting, modelling the laser beam and line shape, calculation of saturation power and fluorescence yield and calculation of detection limits. See DOI: 10.1039/b707394c

analytical laboratory is the determination of Pu, and Pu dosimetry presents a wide range of challenges to an ICP-MS based technique in terms of LOD and specificity. For example, when considering Pu, two parameters must be considered, the dose from β -emission (^{241}Pu) and that from α -emission. Many ICP-MS measurements concentrate on ^{239}Pu and ^{240}Pu , both α -emitters. This may be adequate for monitoring of weapons grade material but, for Pu derived from high burn-up civil fuel, the α -dose from ^{238}Pu can dominate the assessment. A full routine Pu monitoring program must include measurements of all isotopes of interest, including ^{238}Pu and ^{241}Pu . The limits of detection for ^{238}Pu in bioassays are in the region of 4×10^5 atoms dm^{-3} , which is the benchmark with which other techniques should be compared.

The evolution of ICP-MS has seen a steady improvement in the sensitivity of the instruments by about 4 orders of magnitude. Compared to standard radiometric techniques, the determination of radionuclides by ICP-MS is potentially highly favourable, as counting atoms, not radioactive events, leads to a considerable sensitivity bonus for many species of interest. However, for a practical analytical task, this improved sensitivity may not translate directly into enhanced detection limits as the system is limited by either analytical blanks and/or a range of specific and non-specific spectral interferences. In contrast to many “pico–femto trace” measurements, the limitations imposed by an analytical blank can, in many circumstances, be discounted for radionuclide determination by ICP-MS. It is considered that the key to unlocking the undoubted potential of ICP-MS for radionuclide analysis is the control of the background generated by specific or non-specific spectral interferences. The origin of the background in ICP-MS can be assigned to four distinct sources:

1. A non-specific instrumental background that is a function of both the matrix and instrumental factors.
2. Direct mass interference from isotopes of the same nominal mass, *e.g.*, ^{238}U on ^{238}Pu .
3. Direct mass interference from molecular ions of the same nominal mass, *e.g.*, $^{238}\text{U}^1\text{H}^+$ on $^{239}\text{Pu}^+$.
4. Indirect interference from highly abundant species at adjacent masses, *e.g.*, $^{56}\text{Fe}^+$ on $^{55}\text{Fe}^+$.

This paper discusses the potential advantages and limitations of a new means of ion detection in ICP-MS—the use of laser spectroscopy to detect ions as they exit the mass spectrometer. This approach has the potential to significantly attenuate the background signal generated by the non-specific and specific spectral interferences delineated above. This would allow the efficient utilization of the sensitivity bonus offered by ICP-MS over radiometric techniques.

Spectral interferences in ICP-MS

There has been significant progress in the development of techniques for the removal of spectral interferences in ICP-MS. Modification of the sample introduction process to remove the solvent is the simplest approach for matrix related molecular ions and ultimately recourse to separation schemes is available for elemental interferences. These techniques, however, are largely analyte/interferent specific.

High-resolution ($R \leq 11000$), sector-field instruments offer excellent resolution of many of the common molecular ion interferences, but they cannot resolve elemental isobars. Additionally, their abundance sensitivity is limited to 10^{-5} – 10^{-6} for ions at ± 1 D and less for molecular ions with small mass shifts.¹ Thus, adjacent ions at high relative abundance result in systematic error in the determination of rare isotopes.

Collision and reaction cells can address both molecular ions and elemental isobars where appropriate reaction schemes are available.² Isobars can be reduced by up to 9 orders (*e.g.* removal of $^{40}\text{Ar}^+$ on $^{40}\text{Ca}^+$ by reaction with NH_3), but this is restricted to a few elements, most reductions are in the range 3–5 orders (typical of H_2 based reactions). The shifting of mass-to-charge ratios, notably by the use of oxidising agents (O_2 , NO , CO_2) to +16 amu, can be very effective. For example, reactions of U^+ , and UH^+ with CO_2 and its non-reaction with Pu^+ have been reported, enabling the determination of $^{238}\text{Pu}^+$, $^{239}\text{Pu}^+$, $^{240}\text{Pu}^+$, and ^{242}Pu in the presence of 7 orders of magnitude excess uranium matrix.³ Similarly, oxidation of Pu^+ by NO , and the non-reaction of Am^+ , permitted resolution of the isobars of Pu and Am over 2–3 orders of magnitude of relative concentration. The efficiency of such conversions has not, however, been studied in detail. A benefit of this approach is that it provides virtually infinite abundance sensitivity. Unfortunately, the collisions and subsequent reactions introduce additional contributions to the observed mass bias that compromise accurate isotope ratio measurements.⁴

Notwithstanding the considerable advances in the performance of ICP-MS, there are a class of analyses, mostly, but not exclusively involving rare isotopes, where its performance is inadequate. Isobaric interferences at interferent/analyte ratios above 10, where noise considerations dominate, (the 10^9 attenuation quoted above is exceptional for a few isotopes undergoing efficient ion–molecule reactions) and the presence of adjacent isotopes at relative abundances above 10^6 are still largely the province of specialised techniques such as accelerator mass spectrometry (AMS) and resonance ionisation mass spectrometry (RIMS).

For example, for ^{14}C ($t_{1/2} = 5730$ yr), AMS⁵ solves the isobaric interference problem from ^{14}N by generating negative ions such as $^{14}\text{C}^-$, $^{13}\text{CH}^-$, $^{12}\text{CH}_2^-$ (N does not form negative ions readily) by the sputtering of an elemental target. These are then accelerated in a tandem accelerator (0.5–5 MeV) and then collided with a gas or foil stripper to remove H and generate C^{3+} ions for subsequent analysis in a double focussing spectrometer. A typical sample target will contain about 5×10^{19} atoms of ^{12}C , 5.5×10^{17} atoms of ^{13}C and 6×10^7 atoms of ^{14}C yielding a $^{14}\text{C}/^{12}\text{C}$ ratio of 1.2×10^{-12} . Other rare isotopes that can be determined include ^3H ($t_{1/2} = 12.3$ yr), ^7Be (53 d), ^{10}Be (1.5×10^6 yr), ^{26}Al (7.1×10^5 yr), ^{32}Si (140 yr), ^{36}Cl (3.01×10^5 yr), ^{39}Ar (269 yrs), ^{81}Kr (2.3×10^5 yr), ^{85}Kr (10.8 yr), ^{129}I (1.7×10^7 yr) and ^{236}U (2.34×10^7 yr) where the data in brackets indicates the half-life in days or years. The natural abundances of such isotopes are generally in the range 10^{-12} – 10^{-16} . For example, the determination of ^{236}U in sediment samples by AMS has been reported by Marsden *et al.*⁶

Alternatively, RIMS employs 2 or 3 step laser ionisation schemes for highly selective isotopic ionisation followed by mass spectrometric detection.⁷ Isotopic abundance sensitivities of 10^{-13} can be achieved together with detection limits down to 10^6 atoms. Typical applications include $^{238-244}\text{Pu}$, ^{41}Ca and ^{236}U .

Both these techniques are expensive and in the case of AMS require large dedicated laboratories. The major analytical drawback, however, is the need to prepare the analyte in pure form in significant quantity, *e.g.* typically 1 mg for AMS and a few 100 μg coated on to a Ti foil for RIMS.⁸

Outline description of an ICP-MS-CLS instrument

This paper is concerned with exploiting the robustness and versatility of the ICP as an ion source whilst achieving isobaric ion and adjacent ion discrimination at levels approaching those provided by AMS and RIMS. This is accomplished by introducing a high degree of selectivity into the ion detector through the use of laser-induced ionic resonance fluorescence. The conditions, post mass separation, are almost ideal for fluorescence detection in that only a few ionic species are present in the beam and the neutral gas partial pressure is low so that both light scattering and collisional broadening are minimised. In these conditions, high-resolution optical pumping of the desired isotope is readily achieved and the dominant background (BG) comes from adventitious scattering of the laser radiation. Typical values for this BG with good optical design are ~ 50 cps per mW of laser radiation.⁹ Note, in this mode of detection, cw laser excitation is required since the time of arrival of ions in the optical detector window is not known in advance.

A number of approaches to removing the BG scatter are available and they are described below. Fig. 1 shows a diagram of a hypothetical ICP-MS-CLS instrument that employs coincidence laser spectroscopy (CLS) as the principal means of removing scatter, but also allows the use of alternative tech-

niques. The instrument comprises the following units each tailored, as described, to facilitate the optical detection step.

Plasma source and interface

The applications of ICP-MS-CLS demand ultimate performance both in terms of detection and freedom from interference. This indicates a high extraction voltage interface, such as is used in sector-field instruments, as experience suggests that these provide the most efficient ion transport to the mass spectrometer.

A critical design requirement of a CLS spectrometer, as explained below, is to ensure a very low ion energy spread in the region of the optical detector. A shield torch configuration is therefore indicated to de-couple the plasma potential and reduce the energy difference between the plasma and sampler cone. Experiments in this laboratory have shown¹⁰ that reducing the plasma potential does not of itself reduce the ion energy spread, which is the most important parameter, but it does reduce jitter in the potential which is a contributory factor in ion energy spread.

Stage 1—RF ion cooler

Cooling ions and reducing their energy spread is vital for successful operation of the optical detection channel. The ion cooler could be placed prior to the mass separation device (as in collision/reaction cell instruments) which has advantages in improving the performance of the mass separation device, but has the disadvantages of generating additional unwanted species and potentially introducing space-charge effects inside the cooler which might contribute to energy broadening.

The Stage 1 ion cooler would only be an absolute requirement if a high extraction potential interface was used in conjunction with a quadrupole mass filter because the ions would be moving too fast for the quadrupole to operate efficiently. It would not be necessary for a sector instrument. A pressurised rf-only multi-pole can be used as an efficient cooler and a variety of collision gases could be used for heavy ions such as those of the actinides without significant loss of transmission. Problems arise however with scattering losses for light ions such as $^{10}\text{Be}^+$ as fully thermalized ions have no preferential axial velocity. Two approaches to alleviating this problem are available, directed flow of the collision gas² and/or the provision in the cell of an axial field to provide axial acceleration to slow ions.¹¹

Mass spectrometer

The choice between a quadrupole mass filter and a dispersive, sector-field instrument for ICP-MS-CLS is not straightforward and this paper does not offer a definitive statement on this issue.

The dispersive spectrometer in multi-collector configuration does, however, have the considerable benefit of being able to provide simultaneous measurement of major isotopes in conventional detection channels to facilitate isotope ratio measurements and to monitor system performance and stability. A conventional drawback of sector instruments is the loss of transmission associated with narrowing the slits to achieve high resolution $R \geq 400$ performance. This is not an issue for

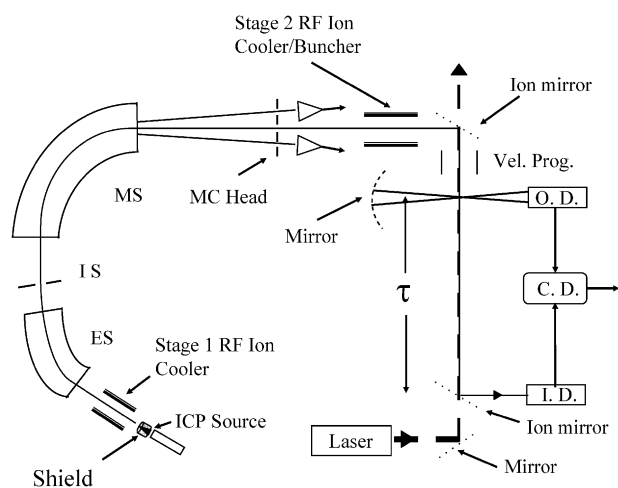


Fig. 1 Schematic of ICP-MS-CLS instrument. ES = electrostatic sector, IS = intermediate slit, MS = magnetic sector, MC = multi-collector, Vel. Prog. = velocity programmer, OD = optical detector, CD = coincidence detector, ID = ion detector, τ = transit time through the flight tube.

CLS detection since approximately unit mass resolution is adequate for sorting ions prior to the optical detector and this is the normal mode of operation in multi-collector systems. Mass calibration stability is, however, very important for CLS because the technique is capable of long (> 10 min) acquisition times and the flat-topped peaks associated with sector instruments provide improved stability compared with quadrupole mass filters.

High performance quadrupoles do have one potentially significant advantage over sector instruments in that their abundance sensitivity is about an order of magnitude better $\sim 10^{-6}$ – 10^{-7} and this might be significant for very rare isotopes at low abundances. In terms of stability and transmission they are however inferior to sector instruments and there is no easy way of providing a simultaneous reference channel to monitor system performance.

Stage 2—RF cooler/buncher

The Stage 2 cooler/buncher is a critical component of the system because ideally, as will be demonstrated, the ion beam has to be cooled to yield an ion energy spread of the order of 0.1–0.2 eV to allow efficient optical pumping. Unpublished work in this laboratory on 3D ion traps has shown that whilst cooling is not difficult, efficient extraction of the ions without energy broadening is more difficult. No specific design work for the Stage 2 cooler is reported here, however, such a device has been described for the IGSOL facility at Jyväskylä.^{12–14} This device employed an rf-only quadrupole, with rods divided into 16 segments to provide an axial field, and an end cap electrode to trap ions for bunching. The function of the buncher is explained in the section on modelling the performance of the CLS detection channel. The trap was operated at pressures of 5×10^{-2} – 10^{-1} mbar. Starting with a 40 keV beam with a 10% energy spread, the final ΔE value was of the order of 0.6 eV. This is certainly higher than required here, but the initial energy spread was of the order of 50–100 eV compared with a few eV for the ICP-MS source.

The optical detector

Optical detection of the ions is the novel step¹⁵ in this design study and therefore the remainder of the paper deals in detail with the modelling of the behaviour of this device.

Coincidence laser spectroscopy for ion detection

CLS is chosen as the preferred mode of detection because it couples optical detection with conventional ion counting thereby offering a dynamic range extending from count rates of much less than 1 cps up to $\sim 3 \times 10^6$ cps. Other than the requirement to work in ion counting mode, a CLS channel does not compromise normal mode ion detection, but takes it into regimes unapproachable by normal means.

Considering only optical detection, CLS is but one of three techniques (CLS, detection of photon multiplicity and ion/photon bunching) for reducing the effect of unwanted photon BG. However, its instrumental configuration enables all three techniques and therefore it is the preferred option for an ICP-MS-CLS instrument.

Instrumentation for CLS

The CLS channel, as shown in Fig. 1, comprises a narrow-band, tuneable, cw-laser propagating co-linearly with, and normally in the opposite direction to the ion beam. Ions enter the optical detector typically at 5–10 kV from a sector instrument, although nuclear experiments generally employ 40 keV¹⁶ source beams. The ions pass through a velocity programmer that is closely coupled with the fluorescence/optical detector. After the optical detector, the ions travel down a flight tube (typically 1 m in length) and are then detected by a conventional ion counter operating in coincidence mode with the optical detector.

The laser. Tuneable lasers are available with outputs throughout the visible and UV parts of the spectrum, but no one laser can cover the whole range of wavelengths required. This is additionally complicated by the requirement for a *continuous wave* (cw) output to allow efficient optical pumping of the discrete and relatively infrequent ions. The duty cycle of a pulsed tuneable system is too low to yield efficient ion detection (*e.g.*, 10 ns at 10^5 Hz = 0.1% duty cycle).

Dye-lasers, pumped by gas or solid-state lasers, offer the widest range of tuneability in the visible and near UV. This flexibility comes at the expense of operational robustness and ease of use, *e.g.*, tuning ranges are relatively narrow and discrete necessitating frequent dye changes to utilize the full wavelength range. Most current CLS systems operate with CW, tuneable dye-lasers, however, in the opinion of the authors they are not robust enough for inclusion in a routine analytical instrument.

Solid state lasers are the preferred choice as they offer much greater reliability and robustness. The best option currently available is to use a diode laser-pumped Ti:sapphire laser followed by frequency doubling. Frequency doubling introduces a consumable element into the laser system (some crystals have limited lifetime), but the technology is well established and widely used in, for example, laser ablation systems. This combination yields mW powers into a 100 KHz bandwidth over the wavelength range from 350–550 nm and this can be further extended using higher harmonics or an optical parametric oscillator (OPO).

Ultimately advances in diode and fibre laser technology are likely to have a major impact on the robustness and cost of the CLS technique, but at present diode tuning ranges are limited to a few nm and therefore several diodes would be needed for a multi-element system.

Velocity programmer. The velocity programmer has two roles in the laser spectrometer. Firstly, to reduce the probability that an ion is optically trapped before entering the optical detector and secondly, to increase or induce an optical isotope shift. Optical trapping occurs when an ion decays to a state that is not radiatively coupled to the ground state. Thus, the ion cannot be re-excited by the laser and emits only one photon. The co-linear geometry of the system introduces the possibility that this single potential detection event could occur outside of the detector volume, *i.e.*, the ion is not detected. The probability of the ion emitting within the detector volume is maximized by tuning the laser off the

“natural” resonance frequency of the ion and using the voltage programmer to accurately and reproducibly accelerate or decelerate the ion using small voltage increments.¹⁷ The consequence of this is that the ion can be Doppler shifted (by the order of a few 10s of MHz) into resonance with the laser only within the confines of the optical detector therefore maximizing the probability of its detection.

Abundance sensitivity in relation to isotopes of the same element is enhanced by the isotope shifts. Isotope shifts are relatively large for either light or heavy elements but lower for many middle mass elements. The voltage programmer can, in conjunction with the acceleration produced in the extraction interface, induce an additional apparent optical isotope by the Doppler process. If ions of adjacent mass are accelerated to the same potential, (*i.e.*, energy), the lighter ion will have a higher velocity than the heavier one and its absorption frequency will be shifted to the blue with respect to that of the heavier ion.

Optical detector. The optical detector, as shown in Fig. 2, comprises a mirror and a fast photon detector, the latter being either a single channel device (conventional photomultiplier) or an imaging detector (imaging photomultiplier¹⁸) that enables the location of photon emission within the detection volume to be determined. The detector must operate in photon counting mode because the detection of a single photon acts as the trigger for timing the coincidence step.

Maximising the optical detection efficiency is vital for the overall detection efficiency. Modelling carried out by APL Ltd (Skipton, UK) suggests that employing an ellipsoidal optic with the beam and detector at the principal foci would yield a collection efficiency of the order of 60–70%. This, combined with a detector quantum efficiency of 30%, indicates that about 20% of the emitted photons might be detected. Higher quantum efficiency can be obtained from CCD detectors, but photon counting requires the photon rate to be less than the reciprocal of the gating time and the readout is not suitable for triggering a fast CLS channel.

Maximising the transit time through the detection volume improves the chance of photon detection, but decreases the effectiveness of the coincidence detector. Employing an imaging detector would provide spatial information on the exact point within the detection volume from which a photon was emitted. This greatly improves coincidence detection and further reduces the impact of isobaric ions or scattered photons. Modelling, however, showed that employing imaging

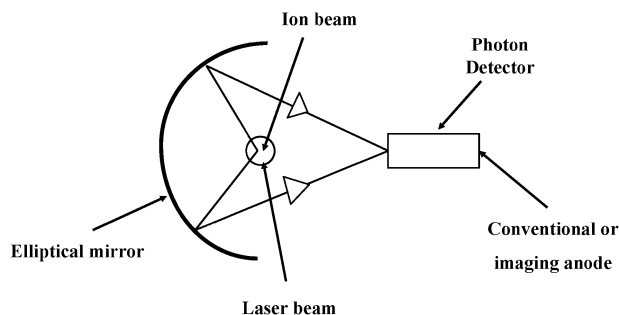


Fig. 2 The optical detector with elliptical reflector.

optics would reduce the optical collection efficiency to about 3% and the overall detection efficiency to about 1%. This option would therefore only be viable for ions that do not undergo optical trapping and can emit a photon burst in the detector volume. Even so, for a 1% optical detection efficiency, 100 photons would be needed to provide unit ion detection efficiency which compares with the 20–50 photons that might typically be emitted by an ion travelling through the 30–50 mm field of view of a practical detector.

A further option is to include more than one optical detector in the line,¹⁹ but again this would only be effective for ions that produce photon bursts and it would add significantly to costs.

Ion counter and coincidence unit. The principal requirement for the ion counter is that it operates at high efficiency, for a discrete dynode device with ions in the 5–10 keV region, ~100% is achievable,²⁰ and with fast counting to maximise the linear range. The coincidence unit is based on standard technology requiring only a programmable delay and acceptance window to record a correlated photon/ion count event.

Modelling the CLS channel and reduction of background

There are 3 basic types of unwanted BG in an ICP-MS spectrum derived, as described in more detail in the Introduction, from isobaric ions, $m/z \pm 1$ ions and scattered photons.

Photon background. Removal or reduction of the BG due to photons is the easiest to deal with and can be achieved by a variety of means depending on the analyte ion being studied. The simplest approach is available for ions that do not undergo optical trapping and can be repetitively pumped by the laser to produce a photon burst as they pass through the optical detection volume. For example a $^{90}\text{Sr}^+$ ion saturated at $\lambda = 421.671 \text{ nm}$ ($5p \ ^2P_{1/2} \rightarrow 5s \ ^2S_{1/2}$), $A = 1.3 \times 10^8 \text{ s}^{-1}$, at 5 keV will take 386 ns to pass through a detection volume 40 mm long and will produce ~50 photons for detection during this period. This is the basis of the “Photon Burst” technique, as described by Fairbank^{21,22} and others,^{23,24} that employs the multiplicity of photon emission to discriminate against BG. The probability of detecting k events in a time τ when the mean count rate is $N \text{ s}^{-1}$ is:

$$P(k, N) = \frac{e^{-N} N^k}{k!} \quad (1)$$

With good optical design a 5 mW laser might produce a BG scatter count of 250 cps and therefore a single ion yielding 1 detected photon in a 1 second count period cannot be detected. However, if the detector is set to record only higher multiplicity events within set time windows, then detection improves rapidly as the multiplicity increases. For example, for a 400 ns detection window, the expected count is $250 \times 400 \times 10^{-9} = 10^{-4}$ and the probability of detecting 1 scatter photon becomes $P(1 \times 10^{-4}) = 10^{-4}$, but there is no way of knowing the origin of a single count. However, if the detector is set to record only higher multiplicity events then for the lowest multiplicity of 2, $P(2 \times 10^{-4}) = 5 \times 10^{-9}$ so there is 2×10^4 less chance that this could have come from the BG and this discrimination improves further with higher multiplicities.

For ions that become trapped and emit only one photon using multiplicity is not an option. However, it is possible to use an “ion buncher”¹⁴ incorporated into the 2nd stage ion cooler to trap the ions for a period and then release them so that the photon output is compressed into a shorter time inducing pseudo multiplicity into the detection scheme. The reduction in BG is determined by:

$$R = \frac{\Delta\tau_{\text{bunch}}}{\tau_{\text{acc}}} \quad (2)$$

Where, $\Delta\tau_{\text{bunch}}$ is the bunching time, or detector transit time in the terminology used above, and τ_{acc} is the accumulation time in the trap. Thus, if the bunching/transit time is $\sim 0.5 \mu\text{s}$ and the accumulation time in the trap is 100 ms, a reduction factor of 5×10^{-6} is achieved so that a 200 photon s^{-1} BG would be reduced to 1 photon per 1000 seconds.

Isobar and $m/z \pm 1$ ion background. Ion detectors have a linear dynamic range extending up to $\sim 3 \times 10^6$ cps, but even with adequate dynamic range, noise considerations limit tolerance of isobars and leakage from ± 1 mass channels to rather low relative abundances ~ 10 (interferent/analyte count ratio). The principal application of CLS is removing these sources of interference, although it removes photon BG as well. Eastham^{19,25} was the first to describe detection of a single fluorescent photon in time correlation with the output from a down-stream, non-specific, ion detector. Whilst only one detection event is needed to trigger the CLS channel, the optical efficiency has to be taken into account. Given an overall photon detection efficiency of $\sim 20\%$, any burst of 5 or more photons should yield 100% efficiency in terms of triggering the CLS channel.

Making the assumption that the counting events are governed by Poisson statistics, and taking into account the excitation characteristics, a Fortran programme “CO-IN” was written that carried out a Monte Carlo simulation of the coincidence detector (see ESI† for a flow chart describing this programme). The inputs of the programme were:

- the mass of the ion,
- the ion energy distribution,
- the length of the optical detection volume,
- the length of the flight tube,
- the cross-sections for absorption and spontaneous emission,
- absorption line-width (based on natural broadening and a Lorentz absorption profile),
- the laser flux density (assuming a continuum source),
- the fraction of ions in the beam that are analyte ions.

The programme outputs were:

- the efficiency of the coincidence detector, that is the number of analyte derived photons that produce a coincidence event,
- the adventitious count rate for the given spurious photon and ion count rates.

The timing diagram for the coincidence detector is shown in Fig. 3. An ion (selected randomly from a Poisson distribution with mean N_T) arrives at some arbitrary time t_1 in the detection volume. If it is an analyte ion (selected according to the specified ratio of analyte to background ions), it is

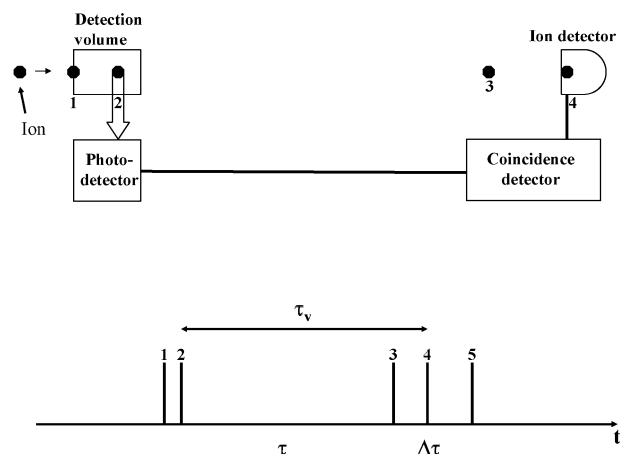


Fig. 3 Timing diagram showing the operation of the coincidence detector.

excited and emits a photon at time t_2 determined by its absorption and emission characteristics. The time $t_2 - t_1$ is generated randomly from the Poisson distribution. The coincidence delay period τ is triggered by the photon and so the coincidence gate is opened for the period $t_3 \rightarrow t_5$. However, the ion is allocated a velocity chosen at random from the specified energy distribution and so covers the flight tube length in a time τ_v arriving at the ion detector at t_4 . If t_4 is within the coincidence window ($\tau \rightarrow \tau + \Delta\tau$), an analyte count is recorded. If the ion is an interfering (background) ion then there is no causal relationship between the detection of a photon (e.g., from scatter) and the ion and so the first ion sampled (which could occur before or after point t_2) is randomly allocated a velocity and its transit time τ_v calculated. Once again detection occurs (in this case a background count) if τ_v places the ion within the coincidence window.

Table 1 provides data on the efficiency of coincidence detection and BG count rates for various ions, ion energy distributions and detector windows. The data show that under a wide range of conditions the majority of the photons emitted from the analyte ions will be counted by the coincidence detector (assuming 100% optical detection efficiency as for ions exhibiting a photon burst). For a 50 mm detection length the efficiency is 100% for all cases, falling to not less than 77% when the detection length is reduced to 5 mm. A significant benefit of reducing the detection length is a significant reduction in the level of spurious counts recorded because of a tightening of the coincidence condition. For example, for 9900 background ions per second and 1000 stray photons per second, the spurious count rate is of the order of 3.4 cps for the 50 mm detection length but falls by an order of magnitude when the detector length is reduced to 5 mm. Changing the flight tube length from 1 to 2 m makes little difference to the performance of the system. A typical operational BG rejection factor would be $\sim 4 \times 10^{-4}$.

Ion energy spread enters critically into the process of optical excitation, but is shown from these calculations to be a secondary consideration in the coincidence detection step.

Note that whilst the CLS mode is very efficient at reducing BG and requires only one photon to trigger the correlation

Table 1 Modelling of the coincidence detector for $^{55}\text{Fe}^+$ Total ion flow = 10 000 cps; analyte fraction = 1%; mean ion energy = 5 keV

$^{55}\text{Fe}^+$			5	50
Length of detection volume $\delta l/\text{mm}$				
Transit time through detector volume $\delta\tau/\text{s}$			3.80×10^{-8}	3.80×10^{-7}
Length of flight tube L/m	Flight time t/s	Stray photon count rate P/cps	True/cps Spurious/cps	True/cps Spurious/cps
$\delta E = 0.1 \text{ eV}$				
$L = 1$	7.61×10^{-6}	50	78.0 0.02	99.9 0.2
		250	78.1 0.1	99.8 0.9
		1000	78.3 0.4	100.0 3.4
$L = 2$	1.52×10^{-5}	50	78.1 0.02	100.0 0.2
		250	78.0 0.09	100.2 0.9
		1000	78.2 0.35	100.1 3.4
$\delta E = 10 \text{ eV}$				
$L = 1$	7.61×10^{-6}	50	74.7 0.02	97.9 0.2
		250	74.7 0.09	98.0 0.9
		1000	75.0 0.329	97.9 3.369
$L = 2$	1.52×10^{-5}	50	69.6 0.02	94.4 0.19
		250	69.7 0.09	94.5 0.9
		1000	69.8 0.3	94.4 3.4

step, all the ions are impinging on the ion detector and so its linear range may be a limiting factor. Practically, however, ICP-MS-CLS is only likely to be used at very low analyte count rates and so pulse pile-up is unlikely to be an operational problem. For photon burst ions or when using a buncher, the ion detector could be turned off and only optical detection employed.

Spectroscopy of selected rare isotopes

The radionuclides of interest that are susceptible to measurement by ICP-MS (which excludes ^3H , ^{14}C , ^{35}S) are dominated by the transition metals (f or d-block). The presence of partly filled d or f shells results in them having complex spectra derived, in some cases, from many thousands of closely spaced energy levels. This complexity is the major determinant of the efficiency of CLS detection because of the following considerations. Efficient pumping requires that the ion is in its ground state energy level before it enters the detection volume. Therefore, low level states must decay or be collisionally depopulated in the ion cooler before entering the optical detection volume. Optical trapping into excited meta-stable levels that are not radiatively coupled to the ground state yields only one fluorescence photon for detection. Odd numbered ions exhibit hyperfine structure that distributes the oscillator strength over several hyperfine lines, only one of

which can be excited without compromising the optical abundance sensitivity.

The isotopes selected here (with some common interferences) are: $^{10}\text{Be}^+$ ($^{10}\text{B}^+ / ^{11}\text{B}^+$), $^{55}\text{Fe}^+$ ($^{55}\text{Mn}^+ / ^{56}\text{Fe}^+$), $^{63}\text{Ni}^+$ ($^{63}\text{Cu}^+ / ^{64}\text{Zn}^+$), $^{90}\text{Sr}^+$ ($^{90}\text{Zr}^+$), $^{99}\text{Tc}^+$ ($^{98}\text{Mo}^+ / ^{99}\text{Ru}^+$), $^{147}\text{Pm}^+$ ($^{147}\text{Sm}^+$), $^{238}\text{U}^+$, $^{238}\text{Pu}^+$ ($^{238}\text{U}^+$) and $^{241}\text{Am}^+$ ($^{241}\text{Pu}^+$) which are representative of those that pose problems for conventional MS techniques. The spectroscopies of these isotopes were obtained from various literature sources,^{26–39} and from application of the COWAN,^{40–42} GRASP92^{43,44} and GraspVU⁴⁵ computer codes.

For each of the ions of interest listed above, the following properties were obtained and are summarized in Fig. 4–11:

E_0 : energy level of the ground state/eV;

E_1 : energy level of the excited state/eV;

λ : wavelength/nm;

A : transition probability/ s^{-1} .

Note that the assignments given in the following sections are for the emission lines, with the upper state term given first. Wavelengths are calculated for consistency throughout directly from the energy levels, but in some cases this results in minor differences in such values and the published data. For example, the $^{55}\text{Fe}^+ - [\text{Ar}] 3d^6 4p \ ^6\text{D}_{9/2} \rightarrow 3d^6 4s \ ^6\text{D}_{9/2}$ has a calculated wavelength of 260.017 nm, but the published²⁶ value is 259.9396 nm. The transition is the definitive identification.

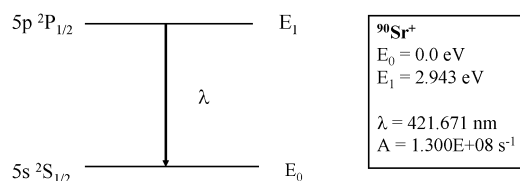


Fig. 4 Energy diagram and atomic parameters for $^{90}\text{Sr}^+$.

$^{90}\text{Sr}^+$ —**Fig. 4**. The electron configuration of Sr^+ is $[\text{Kr}] 5s$, and with only one s electron in its outer shell, it exhibits a simple spectrum typical of the alkali metals. The first available excited state is radiatively coupled to the ground state through the transition $5p \ ^2P_{1/2} \rightarrow 5s \ ^2S_{1/2}$ at $\lambda = 421.671 \text{ nm}$ and has a high transition probability, $A = 1.3 \times 10^8 \text{ s}^{-1}$. There is no hyperfine splitting (even number isotope) or lower lying levels, and therefore the ion can be repetitively pumped with a frequency doubled Ti-sapphire laser and will emit a photon burst as it transits through the detection volume. The $^2P_{1/2}$ state is at 2.94 eV above the ground state and is not significantly populated at the temperatures found in pressurised collision cells or ion traps. Further, its short lifetime means that it will have decayed before it appears in the optical detection volume. Although laser cooling will occur for a repetitively pumped ion, the effect will be small within the detection volume for these fast ions. The transition at 407.770 nm ($5p \ ^2P_{3/2} \rightarrow 5s \ ^2S_{1/2}$), $A = 1.4 \times 10^8 \text{ s}^{-1}$ is even better for CLS, but is just a little further towards the UV.

$^{10}\text{Be}^+$. $^{10}\text{Be}^+$ is of interest to geochemists because it is produced by nuclear spallation of oxygen by cosmic rays and can be used to estimate the weathering rate of rocks. The isobaric interference is from the ubiquitous $^{10}\text{B}^+$. Being a Group II element its spectrum is similar to Sr and there are two excellent transitions for CLS at 313.197 nm ($2p \ ^2P_{1/2} \rightarrow 2s \ ^2S_{1/2}$) with $A = 1.1 \times 10^8 \text{ s}^{-1}$ or 313.041 nm ($2p \ ^2P_{3/2} \rightarrow 2s \ ^2S_{1/2}$) with $A = 1.1 \times 10^8 \text{ s}^{-1}$. There are no lower levels and

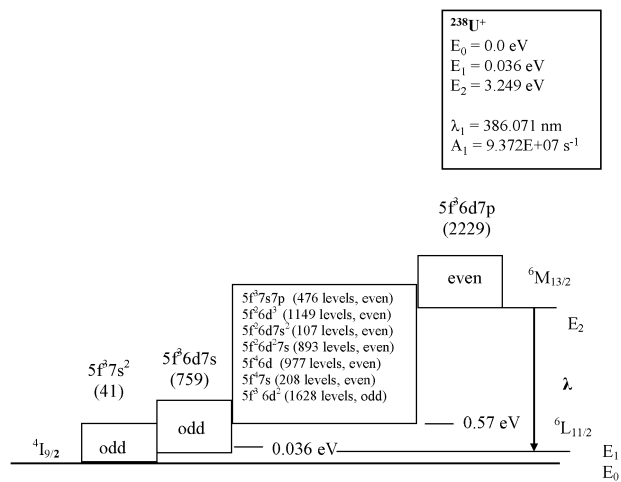


Fig. 5 Energy diagram and atomic parameters for $^{238}\text{U}^+$ (numbers in brackets = number of levels in manifold). Note the first excited state of U^+ is $^6L_{11/2}$ ($E = 0.036 \text{ eV}$). For more details see ref. 56.

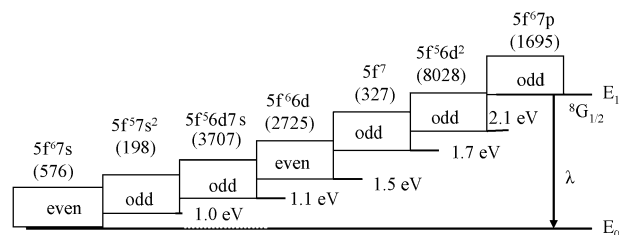


Fig. 6 Energy diagram and atomic parameters for $^{238}\text{Pu}^+$ (numbers in brackets = number of levels in manifold). Note, the first excited state of Pu^+ is $^8F_{3/2}$ ($E = 0.25 \text{ eV}$). For more details, see ref. 35.

so these transitions could be repetitively pumped and provide photon bursts.

$^{238}\text{U}^+$ —**Fig. 5**. The electron configuration of U^+ is $[\text{Rn}] 5f^3 7s^2$ and with an empty $6d$ and partially filled $5f$ shell, it has thousands of energy levels. Further, the simple selection rules that apply to the lighter elements derived from Russell–Saunders coupling break down so that a very large number of transitions can be observed in the spectrum. There are no very strong lines directly coupled to the ground state and the transition $^6K_{9/2} \rightarrow ^4I_{9/2}$ at 428.908 nm has $A = 1.322 \times 10^6 \text{ s}^{-1}$ (estimated value) which is less than ideal for CLS detection ($A_{\text{min}} \sim 5 \times 10^7$). $^6K_{9/2}$ (2.891 eV) is the

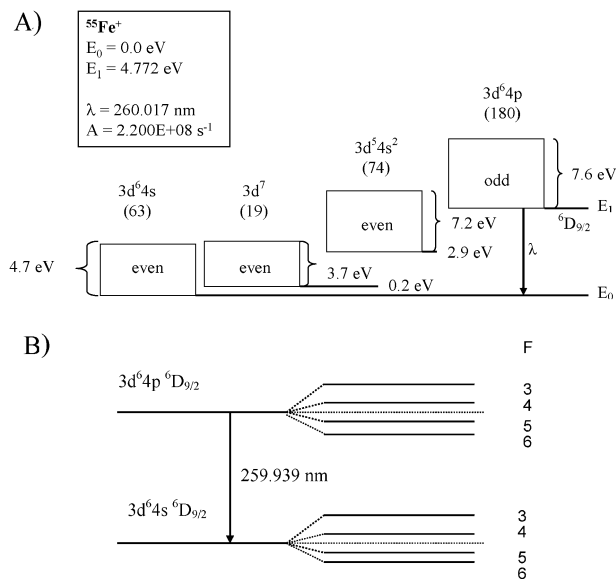


Fig. 7 (A) Energy diagram and atomic parameters for $^{55}\text{Fe}^+$ (numbers in brackets = number of levels in manifold). Note: the first excited state of Fe^+ is $^6D_{7/2}$ ($E = 0.047 \text{ eV}$). For more details, please see ref. 26 and 27 (B) Hyperfine structure for $^{55}\text{Fe}^+$. Approximations of the actual splittings are given in Table 5.

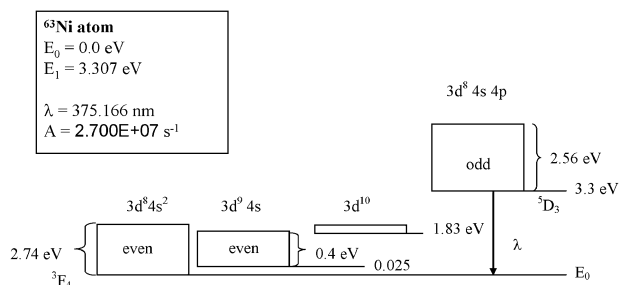


Fig. 8 Energy diagram and atomic parameters for ⁶³Ni atom. Note the first excited state for the atom is at $E = 0.025 \text{ eV}$.

lowest level of $5f^3 7s 7p$, for more details, see ref. 56. This transition is however readily pumped by the Ti-sapphire laser.

There is potentially a more useful line at 386.071 nm , ${}^6\text{M}_{13/2} \rightarrow {}^6\text{L}_{11/2}$, $A = 9.372 \times 10^7$ (see Table 2), but the lower level is the ${}^6\text{L}_{11/2}$ state at 0.036 eV above the ground state. This level will be partly populated at room temperature and thus specific action would be required to cool the ions to maximise the ground state population for resonance transitions. The excited state has even parity and there are odd parity states available for alternative transitions and optical trapping.

Alternatively, the neutral atom has a transition ${}^7\text{M}_6 \rightarrow {}^5\text{L}_6$ at 682.874 nm with $A = 2.2 \times 10^7$ which is readily accessible to solid state lasers without frequency doubling. Alternatively, if frequency doubling is used there is a stronger transition ${}^5\text{L}_7 \rightarrow {}^5\text{L}_6$ at 436.205 nm with $A = 1.3 \times 10^8 \text{ s}^{-1}$. Carrying out the spectroscopy on the neutral atom would require the use of a charge exchange reaction to neutralise the ion. This is readily achievable, as is widely demonstrated in modern collision/reaction cell ICP-MS instruments. The problem, however, is that the resultant neutral atom would have to undergo a free flight to the ion detector and could not be steered by the ion optics. Neutral atoms would therefore most likely need to be detected by optical means only.

Branching from excited states of ²³⁸U. The process in which excited states decay by alternative transitions is known as “branching”, but provided the branched transition results in a photon that can still be detected its effect may not be that significant. The major impact of branching is when optical

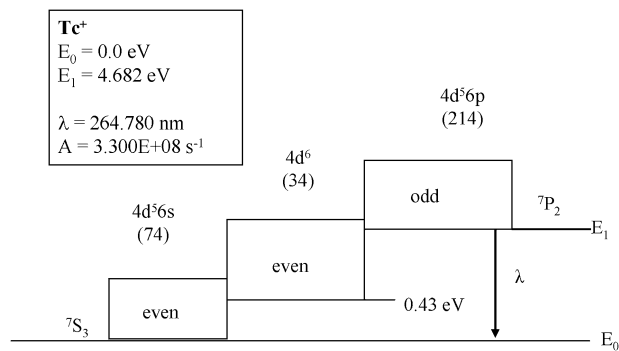


Fig. 9 Energy diagram and atomic parameters for ⁹⁹Tc⁺ (numbers in brackets = number of levels in manifold). Note the first excited state of Tc⁺ is ${}^5\text{D}_4$ ($E = 0.43 \text{ eV}$). For more details, see ref. 26.

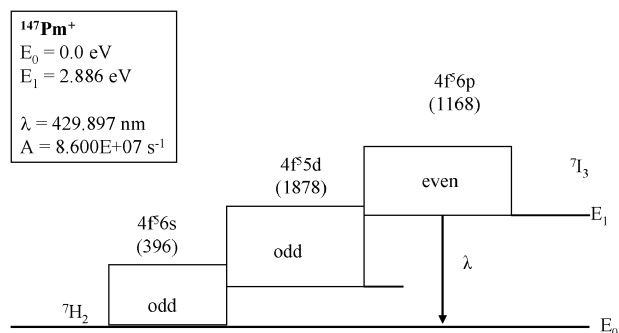


Fig. 10 Energy diagram and atomic parameters for ¹⁴⁷Pm⁺ (numbers in brackets = number of levels in manifold). Note the first excited state of Pm⁺ is ${}^7\text{H}_3$ ($E = 0.055 \text{ eV}$). For more details, see ref. 49.

trapping occurs as this reduces the fluorescence output to one photon and brings into effect the optical detection efficiency which can no longer be compensated by a photon burst. The U⁺ ion is not a good candidate for optical detection, but branching ratios have been estimated for some other ions as described below.

²³⁸Pu⁺—Fig. 6. The Pu⁺ ion has the electron configuration [Rn] $5f^6 7s$. The most useful line appears to be the transition ${}^8\text{G}_{1/2} \rightarrow {}^8\text{F}_{1/2}$ at 453.741 nm (readily accessible with a Ti-sapphire laser) which has $A = 1.22 \times 10^8 \text{ s}^{-1}$.

The excited state has odd parity, but there are both even and odd parity levels available for a radiation cascade back to the ground state. The lowest level above the ground state associated with the $5f^6 7s$ configuration (576 levels) is the ${}^8\text{F}_{3/2}$ term at 0.25 eV . This is advantageous for CLS detection because it is equivalent to a kT temperature of 2903 K and therefore it is unlikely to be populated following ion cooling.

Branching from Pu⁺ ${}^8\text{G}_{1/2}$. The branching ratio for two transitions can be estimated from the ratio of their transition probabilities and for Pu ${}^8\text{G}_{1/2}$ these are shown in Table 3. In this and the subsequent tables the branching ratios were calculated for the summed transition probabilities from a particular configuration. Note the branching ratios are very small and so optical trapping should not be a significant problem for Pu⁺.

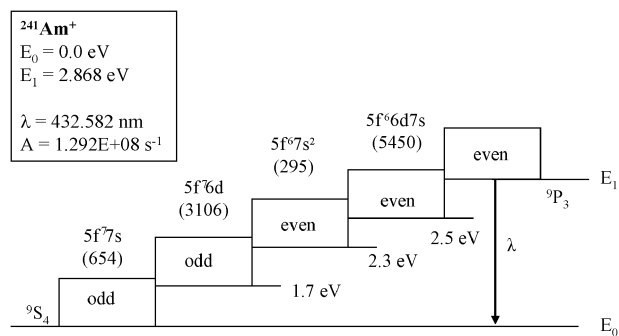


Fig. 11 Energy diagram and atomic parameters for ²⁴¹Am⁺ (numbers in brackets = number of levels in manifold). Note the first excited state of Am⁺ is ${}^7\text{S}_3$ ($E = 0.30 \text{ eV}$). For more details, see ref. 49.

Table 2 Saturation power and fluorescence rate. Laser power $P = 20$ mW, diameter of laser beam $d = 2$ mm, beam cross-section $S = 3.142 \times 10^{-6}$ m², maximum laser intensity $I = 12.73$ kW m⁻², temperature $T = 300$ K

Data	¹⁰ Be ⁺	⁹⁰ Sr ⁺	⁵⁵ Fe ⁺	²³⁸ Pu ⁺	¹⁴⁷ Pm ⁺	²⁴¹ Am ⁺	⁹⁹ Tc ⁺	²³⁸ U ⁺	²³⁸ U	⁶³ Ni ⁺
Mass M/amu	10.00	87.62	55.84	238.00	146.90	241.00	99.00	238.00	238.00	63.00
Energy level E_1/cm^{-1}	0.	0	0	0	0	0	0	289.0	0	0
Statistics weight g_1	2.0	2.0	10.0	2.0	5.0	9.0	7.00	12.0	13.0	9.0
Energy Level $E_2/10^4$ cm ⁻¹	3.193	2.372	3.846	2.204	2.326	2.312	3.777	2.619	1.464	2.665
Statistics weight g_2	4.0	2.0	10.0	2.0	7.0	7.0	5.0	14.0	13.0	7.0
Wavelength $\lambda/10^2$ nm	3.132	4.217	2.600	4.537	4.299	4.326	2.648	3.861	6.829	3.752
Wave number $k/10^4$ cm ⁻¹	3.193	2.372	3.846	2.204	2.326	2.312	3.777	2.590	1.464	2.665
Frequency $\nu/10^{14}$ Hz	9.572	7.110	11.53	6.607	6.974	6.930	11.32	7.765	4.390	7.991
Angular frequency $\omega/10^{15}$ s ⁻¹	6.014	4.467	7.245	4.151	4.382	4.355	7.114	4.879	2.758	5.021
Transition probability $A/10^8$ s ⁻¹	1.100	1.300	2.200	1.219	0.8600	1.292	3.300	0.9372	0.2200	2.700
Doppler width $\Delta\omega_D/10^9$ s ⁻¹	23.59	5.918	12.02	3.337	4.483	3.479	8.867	3.922	2.217	7.845
Natural width $\Delta\omega_N/10^8$ s ⁻¹	1.100	1.300	2.200	1.219	0.8600	1.292	3.300	0.9372	0.2200	2.700
Maximum of Gaussian/ 10^{-10} s	0.3983	1.587	0.7814	2.815	2.095	2.701	1.059	2.395	4.237	1.198
Maximum of Lorentzian/ 10^{-9} s	5.787	4.897	2.894	5.222	7.403	4.927	1.929	6.793	28.94	2.358
Saturation intensity $I_s/10^3$ W m ⁻²	1.490	1.082	7.810	0.814	0.6755	0.9961	11.09	1.016	0.04312	3.191
Saturation power $P_s/10^{-3}$ W	2.340	1.700	12.27	1.279	1.061	1.565	17.43	1.597	0.06773	5.012
Saturation fluorescence rate $R_s/10^7$ s ⁻¹	7.333	6.500	11.00	6.095	5.017	5.653	13.75	5.046	1.100	11.81
Ratio (I/I_s)	8.547	11.77	1.630	15.63	18.85	12.78	1.148	12.53	295.3	3.990
Fluorescence rate $R/10^7$ s ⁻¹	6.565	5.991	6.818	5.729	4.764	5.242	7.348	4.673	1.096	9.445
Small signal case										
Cross-section σ_1 (Lorentzian)/ 10^{-14} m ²	1.561	2.830	1.076	3.277	2.941	2.978	1.116	2.372	7.422	2.240
Cross-section σ_2 (Gaussian)/ 10^{-16} m ²	1.074	9.173	2.906	17.66	8.326	16.32	6.128	8.364	10.87	11.38
Rate of incident photons/ 10^{16} s ⁻¹	6.307	8.491	5.236	9.137	8.656	8.711	5.332	7.774	13.75	7.554
Fluorescence rate $R_1/10^8$ s ⁻¹	3.134	7.648	1.793	9.530	8.105	8.258	1.894	5.870	32.48	5.387
Fluorescence rate $R_2/10^7$ s ⁻¹	0.216	2.479	0.4842	5.137	2.294	4.526	1.040	2.070	4.756	2.736

⁵⁵Fe⁺—**Fig. 7A and B.** The electron configuration of Fe⁺ is [Ar] 3d⁶4s, and with a partially filled d shell, it has a correspondingly complex spectrum. The resonance line ⁶D_{9/2} → ⁶D_{9/2}; at $\lambda = 260.017$ has a transition probability of 2.2×10^8 s⁻¹ which is good for CLS detection. However, the UV wavelength is beyond the range of current solid-state lasers and is only reachable with frequency-doubled, dye-lasers or possibly an OPO. The excited state has odd parity and there are several even parity levels above the ground state where optical trapping could occur. There is a better line at 238.20 nm (3d⁶4p ⁶F_{11/2} → 3d⁶4s ⁶D_{9/2}) with $A = 3.8 \times 10^8$ s⁻¹, but this is even further into the UV.

The lowest energy level of the 3d⁶4s configuration (63 levels up to 8.58 eV) is the ⁶D_{7/2} term at 0.047 eV. This is equivalent to a kT temperature of 546 K and so ion cooling would be necessary to ensure a high population of the ground state.

Branching from Fe⁺ ⁶F_{11/2}. Branching from Fe ⁶F_{11/2} is shown in Table 4. Branching is more significant for Fe⁺

Table 3 Branching ratios for ²³⁸Pu⁺. Transitions from the ⁸G_{1/2} state to:

State	λ/nm	$A_{21}/10^8$ s
5f ⁶ 7s ⁸ F _{1/2}	453.6146	1.220
5f ⁶ 7s	499.2615	1.34×10^4
5f ⁶ 7s	531.6765	8.58×10^4
5f ⁶ 7s	604.5415	3.25×10^4
5f ⁶ 7s	843.6327	2.27×10^4
5f ⁶ 7s	996.5921	1.34×10^4
5f ⁶ 7s	1314.4617	1.40×10^4
5f ⁶ 6d	1999.6706	1.10×10^5
$\alpha(5f^6 7s) = \frac{1.818 \times 10^5}{1.220 \times 10^8} = 1.49 \times 10^{-3}$		
$\alpha(5f^6 6d) = \frac{1.100 \times 10^5}{1.220 \times 10^8} = 9.00 \times 10^{-4}$		

although the competing transitions occur in the UV/visible/NIR and so should be readily detectable.

Hyperfine splitting of Fe⁺ ⁶D_{9/2} → ⁶D_{9/2}. A further complication with ⁵⁵Fe⁺ is the presence of hyperfine splitting (see Fig. 7B and Table 5) due to the odd number of the isotope and its net nuclear spin.⁴⁶ The nuclear spin is weakly coupled to the electronic system, and so does not alter the total radiation of the ion for a given value of the angular momentum J . It does, however, force J into particular orientations with respect to F , thus removing the degeneracy and creating a new set of levels. The absorptive/radiative strength is therefore redistributed over the new levels according to their statistical weights $2F + 1$ (see Kuhn, p. 332).⁴⁷

For the transition of interest $J = 9/2$ and the nuclear spin quantum number $I = 3/2$. The quantum number F takes $2I + 1$ values for $I \leq J$ corresponding to $(J - I)$ to $(J + I)$ in

Table 4 Branching ratios for ⁵⁵Fe⁺. Transitions from ⁶F_{11/2} state to:

State	λ/nm	$A_{21}/10^8$ s
3d ⁶ 4s ⁶ D _{9/2}	238.2039	3.800
3d ⁶ 4s ⁴ H _{9/2}	490.3860	0.015
3d ⁶ 4s ⁴ H _{11/2}	486.7738	0.015
3d ⁶ 4s ⁴ H _{13/2}	482.5736	0.016
3d ⁶ 4s ⁴ F _{9/2}	517.1640	0.013
3d ⁷ ⁴ F _{9/2}	249.3295	0.630
3d ⁷ ² G _{9/2}	382.6900	0.210
3d ⁷ ² H _{9/2}	472.4068	0.120
3d ⁷ ² H _{11/2}	462.2396	0.120
3d ⁵ 4s ²	Forbidden	0.000
$\alpha(3d^6) = \frac{0.059}{3.800} = 1.6 \times 10^{-2}$		
$\alpha(3d^7) = \frac{1.080}{3.800} = 0.284$		
$\alpha(3d^5 4s^2) = 0$		

Table 5 Hyperfine splitting for $^{55}\text{Fe}^+$.

$F_i - F_j$	k/cm^{-1}	λ/nm
3.0–4.0	41 967.9981	238.277
4.0–4.0	41 968.0269	238.277
4.0–5.0	41 968.0230	238.277
5.0–4.0	41 968.0630	238.276
5.0–5.0	41 968.0591	238.276
5.0–6.0	41 968.0544	238.276
6.0–5.0	41 968.1024	238.276
6.0–6.0	41 968.0977	238.276
6.0–7.0	41 968.0923	238.276

$F_i - F_j$	k/cm^{-1}	$\lambda(\text{nm})$
3.0–3.0	38 458.9268	260.018
3.0–4.0	38 458.9238	260.018
4.0–3.0	38 458.9556	260.017
4.0–4.0	38 458.9526	260.017
4.0–5.0	38 458.9487	260.018
5.0–4.0	38 458.9887	260.017
5.0–5.0	38 458.9848	260.017
5.0–6.0	38 458.9802	260.017
6.0–5.0	38 459.0281	260.017
6.0–6.0	38 459.0235	260.017

Splitting of the ground state $E = 0.0 \text{ cm}^{-1}$

F	E_F/cm^{-1}	$\Delta E/\text{eV}$
3.0	0.0595	7.38×10^{-6}
4.0	0.0307	3.80×10^{-6}
5.0	-0.0054	-6.71×10^{-7}
6.0	-0.0487	-6.04×10^{-6}

Splitting of the excited state $E = 38 458.98 \text{ cm}^{-1}$

F	E_F/cm^{-1}	$\Delta E/\text{eV}$
3.0	38 458.9863	7.82×10^{-7}
4.0	38 458.9833	4.03×10^{-7}
5.0	38 458.9794	-7.11×10^{-8}
6.0	38 458.9748	-6.40×10^{-7}

^a Nominal $\lambda = 238.276 \text{ nm}$, $k = 41 968.05 \text{ cm}^{-1}$ (Payling and Larkins:²⁶ $\lambda = 238.2039 \text{ nm}$). Nuclear moment $\mu = -0.635$. Nuclear spin $I = 3/2^-$. Hyperfine splitting constants: ground state $A = -7.21 \times 10^{-3} \text{ cm}^{-1}$. Excited state $A = -7.75 \times 10^{-4} \text{ cm}^{-1}$. ^b Nominal $\lambda = 260.017 \text{ nm}$, $k = 38 458.94 \text{ cm}^{-1}$ (Payling and Larkins:²⁵ $\lambda = 259.9396 \text{ nm}$). Nuclear moment $\mu = -0.635$. Nuclear spin $I = 3/2$. Hyperfine splitting constants: ground state $A = -7.21 \times 10^{-3} \text{ cm}^{-1}$. Excited state $A = -7.65 \times 10^{-4} \text{ cm}^{-1}$.

increments of 1 and $2J + 1$ values for $I \geq J$, the individual terms corresponding to $(I - J)$ to $(I + J)$ in increments of 1. Thus $F = 6, 5, 4, 3$, *i.e.* 4 levels for the both the excited and ground states. The selection rule is that $\Delta F = \pm 1, 0$ with $F = 0$ not allowed. Hence, there are 10 hyperfine components in the pattern.

The hyperfine splittings are calculated from:

$$\Delta E = \frac{1}{2}A[F(F+1) - J(J+1) - I(I+1)] \quad (3)$$

where A is the hyperfine splitting constant (a more detailed account is given in ESI†).

Table 5 shows some calculations of approximate splittings (including additional data for the transition $^6\text{F}_{11/2} \rightarrow ^6\text{D}_{9/2}$ at 238.276 nm), but these ignore contributions from electric quadrupole moments and are presented as an indication of magnitude, exact values would be found from experimenta-

tion. The original level is displaced by only 10^{-5} eV indicating that each of the new levels should be equally populated at ambient temperatures. This leads to uncertainty about the starting level for an ion entering the detection volume.

Considering the relative strengths of the transitions, the Sum Rule states that, within a multiplet, the ratio of the sums of the intensities of all transitions from two states with quantum numbers F and F' are in the ratio of their statistical weights, *i.e.* $(2F + 1):(2F' + 1)$. This implies that the strongest transitions come from the levels with the highest F -number. The intensity ratios of individual line pairs are difficult to calculate, but one line derived from each level tends to dominate, see for example the splitting pattern for the Am atom (see Kuhn p. 334, Plate 14).⁴⁷ Thus, although the oscillator strength for each hyperfine component is a fraction of that for the manifold (as represented by the A value) as a whole, it is not equally divided amongst all the components, but is concentrated in a few lines. Therefore, the effective degradation in A should be restricted to about half the worst case scenario (all 10 lines contributing equally), that is a factor ~ 5 .

⁶³Ni—Fig. 8 (neutral atom shown). The electron configuration of the Ni^+ ion is $[\text{Ar}]3\text{d}^84\text{s}^1$, and as for all the transition metals, the partially filled d orbitals lead to a complex spectrum. The principal resonance lines of Ni^+ occur in the vacuum region of the spectrum at about 120 nm and have very high A values $\sim 6 \times 10^9 \text{ s}^{-1}$, but are completely out of the range of bench-top laser technology. There are no resonance lines above 200 nm and no transitions have been found that are suitable for CLS.

For the ion, Payling and Larkins²⁶ give two terms at 0 and 0.186 eV (kT equivalent = 2160 K) associated with a d^9 configuration, whereas the expected $3\text{d}^84\text{s}^1$ has its lowest level at 1.04 eV extending to 4.03 eV. No resolution to this contradiction is available at this time.

Nickel, as for U, is better detected in the neutral form (and therefore by optical means only) and the neutral energy level diagram is shown in Fig. 8. A strong transition is found at 375.166 nm ($3\text{d}^84\text{s}4\text{p} \ ^5\text{D}_3 \rightarrow 3\text{d}^84\text{s}^2 \ ^3\text{F}_4$), with $A = 2.7 \times 10^8 \text{ s}^{-1}$. The excited state has odd parity and there are two lower lying configurations into which branching/trapping could occur.

The lowest lying level above the ground state of the Ni atom is at 0.025 eV and there are 79 levels associated with the $3\text{d}^84\text{s}^2$ configuration up to a level 2.74 eV. The kT equivalent for this level is only 290 K, which is very low and it would be difficult to avoid thermal population of this level.

Branching from excited states of ⁶³Ni. As for U^+ , Ni^+ does not have convenient lines for optical detection and so branching ratios were not calculated.

Hyperfine splitting of $^5\text{D}_3 \rightarrow ^3\text{F}_4$. Ions similar to ⁶³Ni were examined and it was concluded that the nuclear ground state should have a spin of $\frac{1}{2}$ (note that Stone⁴⁸ quotes a value for the excited state of 5/2). The hyperfine splitting pattern for spin = $\frac{1}{2}$ is:

$$\begin{aligned} ^3\text{F}_4 \text{ term} &\rightarrow F = 9/2, 7/2 = 2 \text{ levels } (2I + 1 = 2) \\ \text{D}_3 \text{ term} &\rightarrow F = 7/2, 5/2 = 2 \text{ levels } (2I + 1 = 2) \end{aligned}$$

Table 6 Hyperfine splitting for $^{63}\text{Ni}^{+a}$

$^{63}\text{Ni}-[\text{Ar}] 3d^8 4s 4p \ ^5D_3 \rightarrow 3d^8 4s^2 \ ^3F_4$		
F_i-F_j	k/cm^{-1}	λ/nm
3.5–2.5	26 654.9241	375.165
3.5–3.5	26 654.9318	375.165
4.5–3.5	26 654.8625	375.166
Splitting of the ground state $E = 0.0 \text{ cm}^{-1}$		
F	E_F/cm^{-1}	
3.5	−0.0385	
4.5	0.0308	
Splitting of the excited state $E = 26\,654.89 \text{ cm}^{-1}$		
F	E_F/cm^{-1}	
2.5	26 654.8856	
3.5	26 654.8933	

^a Nominal $\lambda = 375.166 \text{ nm}$, $k = 26\,654.89 \text{ cm}^{-1}$ (Payling and Larkins²⁶: 374.9044 nm); nuclear moment $\mu = 0.57$ (for an excited state—no data for groundstate); nuclear spin $I = \frac{1}{2}$; hyperfine splitting constants: groundstate $A = 1.54 \times 10^{-2}$; excited state $A = 2.18 \times 10^{-3}$

and a possible 3 transitions in the splitting pattern leading to ~ 2 fold degradation in optical detection efficiency, see Table 6.

$^{99}\text{Tc}^{+}$ —Fig. 9. The electron configuration of the ion is $[\text{Kr}]4d^5 5s$ and the first useful transition is the $4d^5 5p \ ^7P_2 \rightarrow 4d^5 5s \ ^7S_3$ at 264.780 nm for which $A = 3.300 \times 10^8 \text{ s}^{-1}$. This wavelength, as for Fe, is outside of the range currently directly addressable by solid state lasers. The excited state has odd parity and there is an even parity set of levels above the ground state in which optical trapping could occur.

The lowest excited state of the $4d^5 5s$ configuration (74 levels up to 2.98 eV) is the 5D_4 term at 0.43 eV which implies a fully populated ground state in the optical detection volume (kT equivalent to 4994 K).

Branching from $\text{Tc}^{+} \ ^7P_2$. Branching from $\text{Tc} \ ^7P_2$ is shown in Table 7. The effect of branching is likely to be similar to that for Fe and here again the competing transitions occur in the UV/visible and so should be readily detectable.

Hyperfine splitting of $^7P_2 \rightarrow ^7S_3$. ^{99}Tc has a nuclear spin (ground state) of $9/2$. This high value complicates the hyperfine splitting pattern yielding:

Table 7 Branching ratios for $^{63}\text{Tc}^{+}$. Transitions from 7P_2 state to:

State	λ/nm	$A_{21}/10^8 \text{ s}$
$4d^5 5s \ ^7S_3$	264.7011	3.300
$4d^5 5s \ ^5S_2$	397.5017	0.002
$4d^5 5s \ ^5G_2$	717.7381	0.016
$4d^5 5s \ ^5G_3$	721.8207	0.016
$4d^6 \ ^5D_1$	304.7330	0.250
$4d^6 \ ^5D_2$	302.0452	0.260
$4d^6 \ ^5D_3$	297.9753	0.280
$\alpha(4d^5 5s) = \frac{0.034}{3.300} = 1.0 \times 10^{-2}$		
$\alpha(4d^6) = \frac{0.790}{3.300} = 0.239$		

Table 8 Hyperfine splitting for $^{99}\text{Tc}^{+}$

$^{99}\text{Tc}^{+} - [\text{Kr}] 4d^5 5p \ (^7P_2) \rightarrow 4d^5 5s \ (^7S_3)^a$		
F_i-F_j	k/cm^{-1}	λ/nm
1.5–2.5	37 768.1627	264.773
2.5–2.5	37 768.0255	264.774
2.5–3.5	37 768.0104	264.774
3.5–2.5	37 767.8335	264.776
3.5–3.5	37 767.8184	264.776
3.5–4.5	37 767.7990	264.776
4.5–3.5	37 767.5715	264.777
4.5–4.5	37 767.5521	264.778
4.5–5.5	37 767.5283	264.778
5.5–4.5	37 767.2504	264.78
5.5–5.5	37 767.2266	264.78
5.5–6.5	37 767.1985	264.78
6.5–5.5	37 766.8701	264.782
6.5–6.5	37 766.8420	264.783
7.5–6.5	37 766.4305	264.785

Splitting of the ground state $E = 0.0 \text{ cm}^{-1}$

F	E_F/cm^{-1}
1.5	−0.9052
2.5	−0.7680
3.5	−0.5760
4.5	−0.3291
5.5	−0.0274
6.5	0.3291
7.5	0.7406

Splitting of the excited state $E = 37\,767.21 \text{ cm}^{-1}$

F	E_F/cm^{-1}
2.5	37 767.2575
3.5	37 767.2424
4.5	37 767.2230
5.5	37 767.1992
6.5	37 767.1711

^a Nominal $\lambda = 264.776 \text{ nm}$, $k = 37\,767.21 \text{ cm}^{-1}$ (Payling and Larkins²⁶ $\lambda = 264.701 \text{ nm}$); nuclear moment $\mu = 5.6847$; nuclear spin $I = 9/2^{+}$; hyperfine splitting constants: ground state $A = 5.46 \times 10^{-2} \text{ cm}^{-1}$; excited state $A = -4.32 \times 10^{-3} \text{ cm}^{-1}$.

$$^7P_2 \text{ term} \rightarrow F = 13/2, 11/2, 9/2, 7/2, 5/2 = 5 \text{ levels}$$

$$(2J + 1 = 5)^7S_3 \text{ term} \rightarrow F = 15/2, 13/2, 11/2, 9/2, 7/2, 5/2, 3/2 = 7 \text{ levels } (2I + 1 = 7)$$

and a possible 15 transitions in the splitting pattern leading to an ~ 8 fold reduction in the optical detection efficiency (see Table 8).

$^{147}\text{Pm}^{+}$ —Fig. 10. The electron configuration of the ion is $[\text{Xe}] 4f^5 6s$. The transition $^7I_3 \rightarrow ^7H_2$ occurs at 429.897 nm with $A = 8.600 \times 10^7$ and is readily pumped by the Ti-sapphire laser. The excited level has even parity, but an odd parity configuration is available for optical trapping.

The lowest level of the $4f^5 6s$ configuration (396 levels up to 0.83 eV) is the 7H_3 term at 0.055 eV which has an equivalent kT temperature of 639 K. Thus, once again, ion cooling would be necessary to ensure depopulation of this state.

Branching from $\text{Pm}^{+} \ ^7I_3$. Branching from $\text{Pm} \ ^7I_3$ is shown in Table 9. The effect of branching is significant for Pm, but the competing transitions occur in the UV/visible and so should be readily detectable.

Hyperfine splitting of $^7I_3 \rightarrow ^7H_2$. ^{147}Pm has a nuclear spin (ground state) of $7/2$. This high value complicates the hyperfine splitting pattern yielding:⁴⁹

Table 9 Branching ratios for $^{147}\text{Pm}^+$. Transitions from $^7\text{I}_3$ state to:

State	λ/nm	$A_{21}/10^8 \text{ s}$
$4f^5 6s \ ^7\text{H}_2$	429.7777	0.860
$4f^5 6s \ ^5\text{H}_3$	461.5868	0.130
$4f^5 6s \ ^5\text{H}_4$	485.4300	0.120
$4f^5 6s \ ^7\text{F}_2$	567.0930	0.096
$4f^5 6s \ ^7\text{H}_3$	438.1879	0.1300
$4f^5 6s \ ^7\text{H}_4$	451.7925	0.1300
$4f^5 \ 5d \ ^7\text{K}_4$	557.6027	0.099
$\alpha(4f^5 6s) = \frac{0.609}{0.860} = 0.71$		
$\alpha(4f^5 5d) = \frac{0.099}{0.860} = 0.11$		

$^7\text{I}_3$ term $\rightarrow F = 13/2, 11/2, 9/2, 7/2, 5/2, 3/2, \frac{1}{2} = 7$ levels
 $(2J + 1 = 7)^7\text{H}_2$ term $\rightarrow F = 11/2, 9/2, 7/2, 5/2, 3/2 =$
 5 levels ($2I + 1 = 5$)

and a possible 15 transitions in the splitting pattern leading again to potentially an ~ 8 fold reduction in the optical detection efficiency, see Table 10.

$^{241}\text{Am}^+$ —Fig. 11. The americium ion has the electron configuration $[\text{Rn}]5f^7 7s$ and there is a suitable transition for CLS, $^9\text{P}_3 \rightarrow ^9\text{S}_4$ at 432.582 nm (readily accessible to the Ti-sapphire laser). Optical trapping appears to be probable because there is an alternative parity set of levels above the ground state.³⁰

The lowest level of the $5f^7 7s$ configuration (564 levels) is the term $^7\text{S}_3$ at 0.30 eV which has an equivalent kT of 3484 K. This should not be significantly populated after equilibration in a collision cell or trap.

Branching from $^{241}\text{Am}^+ \ ^9\text{P}_3$. Insufficient data was available to estimate branching from $^9\text{P}_3$.

Hyperfine splitting of $^9\text{P}_3 \rightarrow ^9\text{S}_4$. ^{241}Am has a nuclear spin (ground state) of $5/2$. This high value complicates the hyperfine splitting pattern yielding:

$^9\text{P}_3$ term $\rightarrow F = 11/2, 9/2, 7/2, 5/2, 3/2, \frac{1}{2} = 6$ levels
 $(2I + 1 = 6)^9\text{S}_4$ term $\rightarrow F = 13/2, 11/2, 9/2, 7/2, 5/2, 3/2 =$
 6 levels ($2I + 1 = 6$)

and a possible 15 transitions in the splitting pattern as shown in Table 11 (see Kuhn P334 Plate 14⁴⁷ for the splitting pattern of the 432.582 nm line). Once again a worst case is that the optical detection efficiency could be lowered by a factor of ~ 8 .

The above descriptions show that fluorescence detection of ions will work exceptionally well for ions yielding photon bursts, that is for simple 2 level systems having no low lying levels. Efficient pumping requires that all of the ions are in the ground state and available for excitation so an additional concern is that the low lying levels do not remain collisionally populated from the plasma. The ion cooler should in principle de-populate these low lying levels. Ions undergoing optical trapping are detected with lower efficiency and the efficiency is further reduced for odd numbered ions exhibiting hyperfine structure.

Optical pumping of transitions for fluorescence detection

Efficient excitation of spectral transitions is vitally important for fluorescence detection of ions and contributes to the

Table 10 Hyperfine splitting for $^{147}\text{Pm}^+$

$^{147}\text{Pm}^+ - [\text{Xe}]4f^5 6s \ (^7\text{H}_2) - 4f^5 6p \ (^7\text{I}_3)^a$				
$F_i - F_j$	k/cm^{-1}	λ/nm	$k^{(\text{exp})}/\text{cm}^{-1}$	$\lambda^{(\text{exp})}/\text{nm}$
1.5–0.5	23 260.7534	429.909	23 260.9071	429.906
1.5–1.5	23 260.7806	429.908	23 260.9403	429.905
1.5–2.5	23 260.8261	429.907	23 260.9955	429.904
2.5–1.5	23 260.8642	429.907	23 260.9666	429.905
2.5–2.5	23 260.9097	429.906	23 261.0218	429.904
2.5–3.5	23 260.9733	429.905	23 261.0991	429.902
3.5–2.5	23 261.0269	429.904	23 261.0585	429.903
3.5–3.5	23 261.0905	429.902	23 261.1359	429.902
3.5–4.5	23 261.1723	429.901	23 261.2354	429.9
4.5–3.5	23 261.2411	429.9	23 261.1831	429.901
4.5–4.5	23 261.3229	429.898	23 261.2826	429.899
4.5–5.5	23 261.4229	429.896	23 261.4041	429.897
5.5–4.5	23 261.5070	429.895	23 261.3404	429.898
5.5–5.5	23 261.6070	429.893	23 261.4619	429.896
5.5–6.5	23 261.7252	429.891	23 261.6055	429.893

Splitting of the ground state $E = 0.0 \text{ cm}^{-1}$

F	E_F/cm^{-1}
1.5	0.3012
2.5	0.2176
3.5	0.1004
4.5	−0.0502
5.5	−0.2343

Splitting of the excited state $E = 23\,261.30 \text{ cm}^{-1}$

F	E_F/cm^{-1}
0.5	23 261.0546
1.5	23 261.0818
2.5	23 261.1273
3.5	23 261.1909
4.5	23 261.2727
5.5	23 261.3727
6.5	23 261.4909

^a Nominal $\lambda = 429.897 \text{ nm}$, $k = 23\,261.3 \text{ cm}^{-1}$ (payling and larkins:²⁶ $\lambda = 429.781 \text{ nm}$); nuclear moment $\mu = 2.58$; nuclear spin $I = 7/2^+$; hyperfine splitting constants: ground state $A = -3.34 \times 10^{-2} \text{ cm}^{-1}$ ($A^{(\text{exp})} = -1.05 \times 10^{-2} \text{ cm}^{-1}$); excited state $A = 1.81 \times 10^{-2} \text{ cm}^{-1}$ ($A^{(\text{exp})} = 2.21 \times 10^{-2} \text{ cm}^{-1}$) (for experimental data: see ref. 49).

“optical abundance sensitivity” which is combined multiplicatively with the mass abundance sensitivity to give the overall abundance sensitivity of the technique. Maximum fluorescence output is obtained when the transition is saturated and at this point there is no benefit in increasing the laser power as background increases but signal does not. For normal mode detection, there is an additional benefit of saturation in reducing the noise derived from the laser source, but this is not a significant issue in CLS where only one photon is used to trigger the coincidence delay period. Calculation of the minimum saturation intensity is therefore important.

The ions to be detected are in a vacuum and so pressure and Stark broadening can be ignored leaving only a homogeneously broadened line due to the finite lifetime of the excited state. The natural line width is a few 10s of MHz. However, because of the ion energy spread, the centre of the absorption profile of each ion is shifted with respect to the laser frequency, depending on its relative velocity with respect to the laser axis. The ensemble of all ions would be said to be inhomogeneously broadened. Thus, the problem is to ensure that each ion is excited close to the peak of its absorption profile. In this paper, a rather stringent requirement has been applied that the ion is

Table 11 Hyperfine splitting for $^{241}\text{Am}^+$.

$^{241}\text{Am}^+ - [\text{Rn}] 5f^7 7p (^6P_3) \rightarrow 5f^7 7s (^6S_4)^a$		
$F_i - F_j$	k/cm^{-1}	λ/nm
1.5-0.5	23 124.7226	432.438
1.5-1.5	23 124.7174	432.438
1.5-2.5	23 124.7088	432.438
2.5-1.5	23 124.5178	432.441
2.5-2.5	23 124.5092	432.442
2.5-3.5	23 124.4971	432.442
3.5-2.5	23 124.2297	432.447
3.5-3.5	23 124.2176	432.447
3.5-4.5	23 124.2021	432.447
4.5-3.5	23 123.8583	432.454
4.5-4.5	23 123.8428	432.454
4.5-5.5	23 123.8238	432.454
5.5-4.5	23 123.4036	432.462
5.5-5.5	23 123.3846	432.463
6.5-5.5	23 122.8656	432.472

Splitting of the ground state $E = 0.0 \text{ cm}^{-1}$

F	E_F/cm^{-1}
1.5	-0.9981
2.5	-0.7985
3.5	-0.5190
4.5	-0.1597
5.5	0.2795
6.5	0.7985

Splitting of the excited state $E = 23\,123.69 \text{ cm}^{-1}$

F	E_F/cm^{-1}
0.5	23 123.7245
1.5	23 123.7193
2.5	23 123.7107
3.5	23 123.6986
4.5	23 123.6831
5.5	23 123.6641

^a Nominal $\lambda = 432.582 \text{ nm}$, $k = 23\,123.69 \text{ cm}^{-1}$ (literature value 429.781 nm , see ref. 29); nuclear moment $\mu = 1.61$; nuclear spin $I = 5/2^-$; hyperfine splitting constants: ground state $A = 7.98 \times 10^{-2} \text{ cm}^{-1}$; excited state $A = -3.45 \times 10^{-3} \text{ cm}^{-1}$.

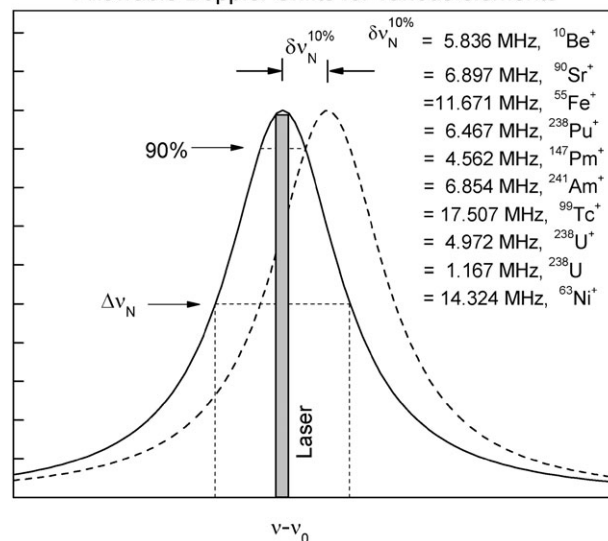
probed within the range where its absorption coefficient is within 10% of its peak value. It will be demonstrated that this requires a significant reduction in the ion energy spread typically produced in ICP-MS instruments.

Because of the limited abundance sensitivity of conventional mass spectrometers, intense ion beams at masses $M \pm 1$ will result in ions of the same element being present in the CLS channel at mass M . The degree to which such ions will be excited and contribute erroneously to the measured signal will depend on 2 factors: the isotope shift and the differential velocity (and resultant frequency shift) that ions of different mass reach when accelerated through the same field. Additionally, and overlaying these effects, is the phenomenon known as Doppler compression which reduces the effect of ion energy spread when ions are accelerated to high velocity.

Doppler compression and its effect on ion energy spread

It can be shown that¹⁶

$$\Delta\nu_D = \nu_0 \frac{\Delta E}{\sqrt{(2eUm c^2)}} \quad (4)$$

Allowable Doppler Shifts for various elements**Fig. 12** Schematic showing the maximum Doppler Shifts that allow excitation within 10% of the absorption maximum.

Where

$\Delta\nu_D$ is the Doppler frequency spread,

ν_0 is the centre frequency,

ΔE the ion energy spread,

e the charge on the electron,

U the voltage,

m the mass of the ion,

c the velocity of light.

To ensure efficient pumping with minimum laser power the criterion set here, as indicated above, is that the laser should pump the transition within the range $\Delta\nu_N^{10\%}$ such that its absorption coefficient is within 10% of its peak value, this principle is illustrated in Fig. 12. Fig. 13A–J show the allowed Doppler shifts $\Delta\nu_D^{10\%}$ associated with a range of ion energy spreads for different acceleration voltages for the isotopes $^{10}\text{Be}^+$, $^{55}\text{Fe}^+$, $^{90}\text{Sr}^+$, $^{238}\text{U}^+$, ^{238}U , ^{238}Pu , ^{63}Ni , ^{99}Tc , ^{147}Pm and ^{241}Am which cover a wide mass range and range of transition probabilities (A values). The relevant data are presented in Table 12. Note that because the natural width is inversely proportional to the A value, transitions that are highly suitable for CLS (high A values) also readily meet the Doppler shift criterion, this is clearly indicated comparing the $^{238}\text{U}^+$ ion to the ^{238}U atom.

The data show that for efficient optical pumping, ion energy spread needs to be $<0.5 \text{ eV}$ and preferably $\sim 0.1 \text{ eV}$. Reducing the normally encountered ion energy spread of a few eV (see Douglas and Tanner in ref. 1 also ref. 10) to the order of 0.1 eV represents a technical challenge and requires development of the second stage ion cooler. Tanner has reported² that currently used collision/reaction cells offer pseudo equilibrium energies of $\sim 0.1 \text{ eV}$, however, there is an additional contribution of $\sim 0.8 \text{ volts}$ from the rf drive which is in the radial direction (which is not significant for co-linear on-axis optical pumping) that could be partitioned to axial modes in a pressurised cell such as might be used for metastable quenching.

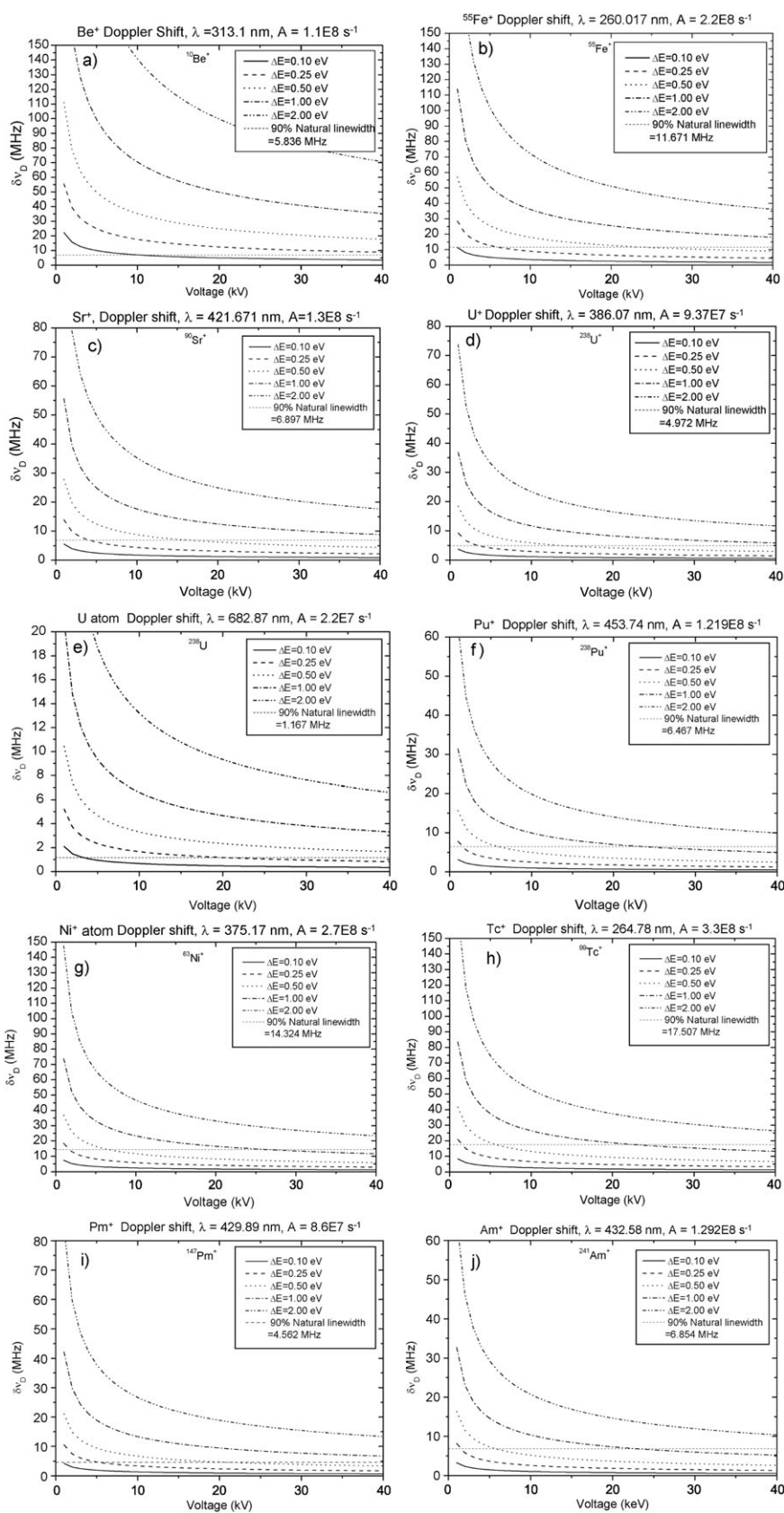


Fig. 13 (A) Doppler shifts associated with a range of ion energy spreads for different acceleration voltages for: (a) $^{10}\text{Be}^+$, (b) $^{55}\text{Fe}^+$, (c) $^{90}\text{Sr}^+$, (d) $^{238}\text{U}^+$, (e) ^{238}U atom, (f) $^{238}\text{Pu}^+$, (g) $^{63}\text{Ni}^+$ atom, (h) $^{99}\text{Tc}^+$ atom, (i) $^{147}\text{Pm}^+$, (j) $^{241}\text{Am}^+$.

Table 12 Maximum ion energy spreads for the allowed Doppler shifts $\Delta\nu_D^{10\%}$ at various ion energies

Ion	λ/nm	A/s^{-1}	$\Delta\nu_D^{10\%}/\text{MHz}$	$\Delta E_{\text{max}}/\text{eV}$	
				@ 5 keV	@ 20 keV
$^{10}\text{Be}^+$	313.197	1.1×10^8	5.84	<0.1	0.1
$^{55}\text{Fe}^+$	260.017	2.2×10^8	11.67	0.25	0.4
$^{90}\text{Sr}^+$	421.671	1.3×10^8	6.90	0.25	0.5
$^{238}\text{U}^+$	386.071	9.37×10^7	4.97	0.25	0.5
^{238}U	682.874	2.2×10^7	1.17	0.1	0.25
$^{238}\text{Pu}^+$	453.741	1.2×10^8	6.47	~0.5	~0.8
^{63}Ni	375.166	2.7×10^8	14.32	~0.4	~0.8
$^{99}\text{Tc}^+$	264.780	3.3×10^8	17.51	0.5	1.0
$^{147}\text{Pm}^+$	429.897	8.6×10^7	4.56	0.25	0.5
$^{241}\text{Am}^+$	432.582	1.3×10^8	6.85	~0.5	~1.0

Transverse optical excitation of the ion beam (to avoid the axial energy spread) is an alternative option, but has two drawbacks. Firstly, the laser power required is greatly increased because the target area is that of the projection of a 2 mm diameter by 50 mm long cylinder compared with the cylindrical cross-section of the ion beam. Secondly, voltage programming, which is a simple and efficient means of bringing the ions into resonance, enables the laser to be stabilised and locked to an accurately known frequency and importantly allows the induction of an apparent isotope shift, would be excluded.

Calculation of the optical abundance sensitivity (AS). Limited abundance sensitivity is one of the major problems encountered in the measurement of low abundance isotopes. For example, $^{55}\text{Fe}^+$ is isobaric with ^{55}Mn and sits one mass unit away from the major isotope of ubiquitous natural iron $^{56}\text{Fe}^+$ and in addition to this, $^{56}\text{ArO}^+$ is a major spectral component in ICP-MS spectra. ICP-MS-CLS combines the abundance sensitivity of both the mass selective and optical processes. Although a small fraction (10^{-4} – 10^{-5} low mass side) of the $M \pm 1$ isotopes will be present in the optical detector at the same time as the analyte ion, these isotopes do not absorb at the same wavelength, even for ions of the same element at rest.

Acceleration of the ions produces a further differential wavelength shift due to the Doppler effect.

The isotope shift for isotopes of the same element is given by, $\delta\omega_i = \delta\omega^{(m)} + \delta\omega^{(v)}$ and is calculated with help of the two following formulas. These provide an estimate of the magnitude of the shift, but exact values would be determined by experimentation.

- Mass effect on the isotope shift $\delta\omega^{(m)}$:

$$\delta\omega^{(m)} = -\frac{\omega}{1 - \frac{m}{M_B}} \frac{m\delta M}{M_B M_A} \quad (5)$$

where ω is the frequency of the transition for isotope with mass M_B . The frequency of the transition for isotope with mass M_A (where $M_A > M_B$) is $\omega^* = \omega + \delta\omega^{(m)}$, where m is the electron mass and $\delta M = M_B - M_A$.

Volume effect on isotope shift $\delta\omega^{(v)}$:

$$\delta\omega^{(v)} = \frac{1}{(4\pi\epsilon_0)^2} \frac{me^4}{\hbar^3} \frac{4Z_a^2}{n_*^3} \frac{1 + \gamma}{[\Gamma(2\gamma + 1)]^2} B(\gamma) \left(\frac{2Zr_0}{a_0}\right)^{2\gamma} \frac{\delta r_0}{r_0} \quad (6)$$

Where

ϵ_0 is the permittivity of free space

Z and Z_a the atomic number and charge on the ion core, respectively

m is the mass

n^* the effective quantum number

$\gamma = \sqrt{1 - \alpha^2 Z^2}$ with α the fine structure constant $a_0 = \frac{\hbar^2}{me^2} = 5.2910^{-11} \text{m}$

$\Gamma(2\gamma + 1)$ is the gamma function of argument $(2\gamma + 1)$ defined by $\Gamma(z) = \int_0^\infty t^{z-1} e^{-t} dt$.

Taking into account that the charge is distributed over the whole volume of nucleus, the factor B is given by the expression:

$$B(\gamma) = \frac{3}{(2\gamma + 1)(2\gamma + 3)} \quad (7)$$

and

r_0 is the radius of the nucleus, estimated as $r_0 = 1.2 \times 10^{-13} M^{\frac{1}{3}} \text{cm}$.

Thus for two isotopes A and B, at masses M_A and M_B the spectral lines for B will be shifted with respect to A according to the equation $\omega_B = \omega_A + \delta\omega_i$. If additionally they are moving with the same energy E , their spectral lines will be shifted relative to each other because of the Doppler effect.

$$\delta\omega_D^A = \frac{1}{c} \sqrt{\frac{2E}{M_A}} \omega^A \quad (8)$$

$$\delta\omega_D^B = \frac{1}{c} \sqrt{\frac{2E}{M_B}} \omega^B \quad (9)$$

The differential Doppler shift in absolute frequency units is therefore:

$$\Delta\delta\omega_D = |(\delta\omega_D^B - \delta\omega_D^A)| \neq 0 \quad (10)$$

The quantity $\Delta\delta\omega_D$ is tabulated in Table 13 (for ions at 5 keV).

The total shift, as illustrated in Fig. 14, between the two isotopes is given by:

$$\Delta\omega = \omega^B - \omega^A = (\delta\omega_D^B - \delta\omega_D^A) + \delta\omega_i \quad (11)$$

Note that in eqn (11), the relative Doppler shift is always expressed as the difference between the lighter and heavier isotope which is always a positive quantity. However, in Table 13 the isotope shifts are always calculated with respect to the centre isotope. For this reason the total shift for light \rightarrow heavy isotope is given by eqn (11), whereas for the heavy \rightarrow light situation

$$\Delta\omega = -((\delta\omega_D^B - \delta\omega_D^A) - \delta\omega_i) \quad (12)$$

Table 13 Calculation of the optical abundance sensitivity for various isotopes

Isotope	Isotope shift $\delta\omega_i/\text{MHz}$	Doppler shift $\delta\omega_D/\text{MHz}$	Relative doppler shift $\Delta\delta\omega_i/\text{MHz}$	Total shift $\Delta\omega_i/\text{MHz}$	Optical shift $\Delta\lambda_i/\text{nm}$ (based on $\delta\omega_i$)	Optical shift $\Delta\lambda_i/\text{nm}$ (based on $\Delta\omega$)	Total optical shift $\Delta\nu$ bar/ cm^{-1} (based on $\Delta\omega$)	Total optical shift $\delta\lambda_i/\text{nm}$	Optical abundance sensitivity
$^{10}\text{Be}^+$									
$\lambda = 313.197 \text{ nm}$									
8	-8.09×10^4	6.97×10^6	7.35×10^5	6.55×10^5	4.21×10^{-3}	-3.41×10^{-2}	-3.47	4.21×10^{-3}	4.62×10^{-7}
9	-3.59×10^4	6.57×10^6	3.37×10^5	3.01×10^5	1.87×10^{-3}	-1.57×10^{-2}	-1.60	1.87×10^{-3}	2.35×10^{-6}
10		6.23×10^6							
11	2.92×10^4	5.94×10^6	-2.90×10^5	-2.61×10^5	-1.52×10^{-3}	1.36×10^{-2}	1.38	-1.52×10^{-3}	3.55×10^{-6}
12	5.34×10^4	5.69×10^6	-5.43×10^5	-4.89×10^5	-2.78×10^{-3}	2.55×10^{-2}	2.60	-2.78×10^{-3}	1.06×10^{-6}
$^{55}\text{Fe}^+$									
$\lambda = 260.071 \text{ nm}$									
53	3.85×10^4	3.26×10^6	5.98×10^4	9.83×10^4	-1.38×10^{-3}	-3.52×10^{-3}	-5.22×10^{-1}	-1.38×10^{-3}	8.17×10^{-6}
54	1.93×10^4	3.23×10^6	2.95×10^4	4.88×10^4	-6.91×10^{-4}	-1.75×10^{-3}	-2.59×10^{-1}	-6.92×10^{-4}	3.26×10^{-5}
55		3.20×10^6							
56	-1.93×10^4	3.17×10^6	-2.87×10^4	-4.80×10^4	6.93×10^{-4}	1.72×10^{-3}	2.55×10^{-1}	6.93×10^{-4}	3.24×10^{-5}
57	-3.87×10^4	3.14×10^6	-5.67×10^4	-9.54×10^4	1.39×10^{-3}	3.42×10^{-3}	5.06×10^{-1}	1.39×10^{-3}	8.08×10^{-6}
$^{90}\text{Sr}^+$									
$\lambda = 421.671 \text{ nm}$									
88	5.46×10^4	1.56×10^6	1.75×10^4	7.21×10^4	-5.15×10^{-3}	-6.80×10^{-3}	-3.82×10^{-1}	-5.16×10^{-3}	1.42×10^{-6}
89	2.73×10^4	1.55×10^6	8.65×10^3	3.60×10^4	-2.58×10^{-3}	-3.39×10^{-3}	-1.91×10^{-1}	-2.58×10^{-3}	5.66×10^{-6}
90		1.54×10^6							
91	-2.73×10^4	1.53×10^6	-8.51×10^3	-3.58×10^4	2.58×10^{-3}	3.38×10^{-3}	1.90×10^{-1}	2.58×10^{-3}	5.66×10^{-6}
92	-5.47×10^4	1.53×10^6	-1.69×10^4	-7.15×10^4	5.15×10^{-3}	6.75×10^{-3}	3.80×10^{-1}	5.16×10^{-3}	1.41×10^{-6}
$^{99}\text{Tc}^+$									
$\lambda = 264.780 \text{ nm}$									
97	1.28×10^5	2.37×10^6	2.41×10^4	1.52×10^5	-4.74×10^{-3}	-5.64×10^{-3}	-8.05×10^{-1}	-4.75×10^{-3}	1.67×10^{-6}
98	6.38×10^4	2.35×10^6	1.19×10^4	7.57×10^4	-2.37×10^{-3}	-2.82×10^{-3}	-4.02×10^{-1}	-2.37×10^{-3}	6.69×10^{-6}
99		2.34×10^6							
100	-6.38×10^4	2.33×10^6	-1.18×10^4	-7.56×10^4	2.37×10^{-3}	2.81×10^{-3}	4.01×10^{-1}	2.37×10^{-3}	6.69×10^{-6}
101	-1.28×10^5	2.32×10^6	-2.34×10^4	-1.51×10^5	4.74×10^{-3}	5.61×10^{-3}	8.01×10^{-1}	4.75×10^{-3}	1.67×10^{-6}
$^{147}\text{Pm}^+$									
$\lambda = 429.897 \text{ nm}$									
145	2.56×10^5	1.19×10^6	8.21×10^3	2.64×10^5	-2.50×10^{-2}	-2.59×10^{-2}	-1.40	-2.51×10^{-2}	2.83×10^{-8}
146	1.28×10^5	1.19×10^6	4.08×10^3	1.32×10^5	-1.25×10^{-2}	-1.29×10^{-2}	-7.00×10^{-1}	-1.25×10^{-2}	1.13×10^{-7}
147		1.18×10^6							
148	-1.28×10^5	1.18×10^6	-4.04×10^3	-1.32×10^5	1.25×10^{-2}	1.29×10^{-2}	6.99×10^{-1}	1.25×10^{-2}	1.13×10^{-7}
149	-2.56×10^5	1.18×10^6	-8.04×10^3	-2.64×10^5	2.50×10^{-2}	2.58×10^{-2}	1.40	2.51×10^{-2}	2.83×10^{-8}
$^{238}\text{U}^+$									
$\lambda = 386.071 \text{ nm}$									
236	2.64×10^6	1.04×10^6	4.94×10^3	2.65×10^6	-2.09×10^{-1}	-2.09×10^{-1}	-1.40×10^1	-2.09×10^{-1}	3.15×10^{-10}
237	1.32×10^6	1.04×10^6	2.46×10^3	1.32×10^6	-1.04×10^{-1}	-1.05×10^{-1}	-7.02	-1.04×10^{-1}	1.26×10^{-9}
238		1.04×10^6							
239	-1.32×10^6	1.03×10^6	-2.45×10^3	-1.32×10^6	1.04×10^{-1}	1.05×10^{-1}	7.02	1.05×10^{-1}	1.26×10^{-9}
240	-2.64×10^6	1.03×10^6	-4.89×10^3	-2.65×10^6	2.09×10^{-1}	2.09×10^{-1}	1.40×10^1	2.09×10^{-1}	3.15×10^{-10}

Table 13 (continued)

Isotope	Isotope shift $\delta\omega_i/\text{MHz}$	Doppler shift $\delta\omega_D/\text{MHz}$	Doppler shift $\Delta\omega_D/\text{MHz}$	Relative doppler shift $\Delta\delta\omega/\text{MHz}$	Total shift $\Delta\omega/\text{MHz}$	Optical shift $\Delta\lambda/\text{nm}$ (based on $\delta\omega_i$)	Optical shift $\Delta\lambda/\text{nm}$ (based on $\Delta\omega$)	Total optical shift cm^{-1} (based on $\Delta\omega$)	Total optical shift $\Delta\nu/\text{bar}$ (based on $\Delta\omega$)	Total optical shift $\delta\lambda/\text{nm}$	Optical abundance sensitivity
$^{238}\text{Pu}^+$											
$\lambda = 453.741 \text{ nm}$											
236	2.99×10^6	8.86×10^5	4.37×10^3	2.99×10^6	-3.26×10^{-1}	-3.27×10^{-1}	-1.59×10^1	-3.26×10^{-1}	-1.63×10^{-1}	-3.26×10^{-1}	4.16×10^{-10}
237	1.49×10^6	8.84×10^5	2.18×10^3	1.50×10^6	-1.63×10^{-1}	-1.63×10^{-1}	-7.93	-1.63×10^{-1}	-1.63×10^{-1}	-1.63×10^{-1}	1.67×10^{-9}
238		8.82×10^5									
239	-1.49×10^6	8.80×10^5	-2.16×10^3	-1.50×10^6	1.63×10^{-1}	1.63×10^{-1}	7.93	1.63×10^{-1}	1.63×10^{-1}	1.63×10^{-1}	1.67×10^{-9}
240	-2.99×10^6	8.78×10^5	-4.31×10^3	-2.99×10^6	3.26×10^{-1}	3.27×10^{-1}	1.59×10^1	3.27×10^{-1}	3.27×10^{-1}	3.27×10^{-1}	4.16×10^{-10}
$^{241}\text{Am}^+$											
$\lambda = 432.582 \text{ nm}$											
239	3.67×10^6	9.24×10^5	4.62×10^3	3.68×10^6	-3.64×10^{-1}	-3.65×10^{-1}	-1.95×10^1	-3.64×10^{-1}	-3.64×10^{-1}	-3.64×10^{-1}	3.10×10^{-10}
240	1.84×10^6	9.22×10^5	2.30×10^3	1.84×10^6	-1.82×10^{-1}	-1.82×10^{-1}	-9.75	-1.82×10^{-1}	-1.82×10^{-1}	-1.82×10^{-1}	1.24×10^{-9}
241		9.19×10^5									
242	-1.84×10^6	9.17×10^5	-2.29×10^3	-1.84×10^6	1.82×10^{-1}	1.82×10^{-1}	9.75	1.82×10^{-1}	1.82×10^{-1}	1.82×10^{-1}	1.24×10^{-9}
243	-3.67×10^6	9.15×10^5	-4.56×10^3	-3.68×10^6	3.64×10^{-1}	3.65×10^{-1}	1.95×10^1	3.65×10^{-1}	3.65×10^{-1}	3.65×10^{-1}	3.10×10^{-10}

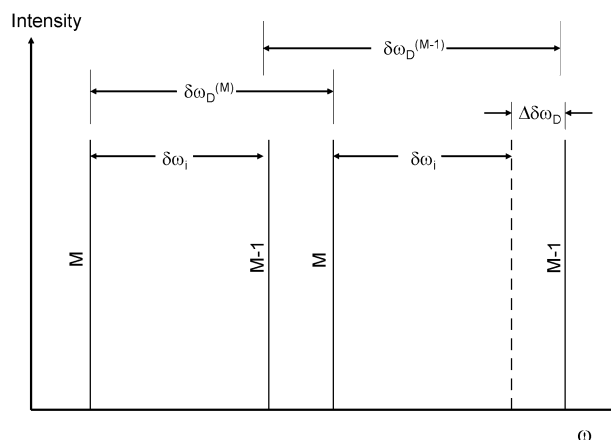


Fig. 14 Diagram showing how the total isotope shift $\Delta\omega$ is estimated.

Algebraically they are the same, but the logic is clearer if eqn (12) is expressed in this form.

The optical component of the abundance sensitivity derived from calculating the absorption coefficient at $\Delta\omega$ relative to that at the line centre is given in Table 13. Note that the relative Doppler shift is, as expected, large for the lightest isotopes, of the order of 300 GHz per mass unit for Be^+ compared with 2.3 GHz per mass unit for Am^+ . Conversely, the isotope shift is low at the low-mass end of the spectrum, of the order of 30 GHz per mass unit for Be^+ , dominated by the relative mass effect, but increases to 1800 GHz at the high mass end (Am^+) due to the volume effect. This leads to optical abundance sensitivities in the range 10^{-5} – 10^{-9} .

The overall abundance sensitivity is the product of the optical and mass spectroscopic abundance sensitivity. Given typical values of 10^{-5} for the mass spectroscopy, the overall value varies from $\sim 10^{-10}$ for the light isotopes to $\sim 10^{-14}$ for heavy isotopes.

A bibliography on experimental optical isotope shifts has been published by Heilig.⁵¹

Calculation of the saturation flux and fluorescence yield. The natural line shape which is relevant to ions in a vacuum can be described by the normalised function:

$$g_N(\omega - \omega_0) = \frac{1}{2\pi\tau} \frac{1}{(\omega - \omega_0)^2 + (\frac{1}{2\tau})^2} \equiv \frac{2}{\pi\Delta\omega_N} \frac{1}{1 + (\frac{\omega - \omega_0}{\Delta\omega_N/2})^2} \quad (13)$$

where τ is the lifetime of the excited state.

The central value of this function when $\omega = \omega_0$ is given by:

$$g_N(0) = \frac{2\tau}{\pi} \equiv \frac{2}{\pi\Delta\omega_N} \quad (14)$$

And half width is given by:

$$\Delta\omega_N = \frac{1}{\tau} = A_{ki} \quad (15)$$

This leads to a value for the absorption cross-section at the line centre of:

$$\sigma_N = \left(\frac{\lambda}{2}\right)^2 \frac{g_N(0)}{\tau} = \frac{\lambda^2}{2\pi} \quad (16)$$

Thus at 600 nm σ_N is $4 \times 10^{-14} \text{ m}^2$. The rate of pumping such a transition per second is given by:

$$R = \sigma_N I_P \quad (17)$$

Where I_P is the intensity here measured in photons m^{-2} .

For a typical excited state lifetime of 10^{-8} s , saturation occurs if the pumping rate exceeds the decay rate so $R > 1/\tau$. Thus $I > 2.74 \times 10^{21}$ photons per second or 0.9 mW mm^{-2} for a 1 mm cross sectional area beam. Formally the approximate saturation intensity is given by:

$$I_s = \frac{\pi h c}{3\lambda^3 \tau} \quad (18)$$

Application of this equation shows that most useful transitions in the UV/visible part of the spectrum can be saturated at powers of $< 2 \text{ mW}$ which is quite modest and readily provided by modern tuneable laser systems. The exact calculations shown below take into account line profiles and show higher, but still readily attainable, powers and there is a balance to be struck between achieving saturation and increasing the non-specific background due to scattering of the laser beam.

Actual pumping efficiency is determined by the overlap between the absorption line and the laser line profile. The laser profile is defined by:

$$\int_0^\infty f(\omega - \omega_1) d\omega = 1 \quad (19)$$

Examples:

(1) The laser approximates a monochromatic source with circular frequency ω_1 in which case

$$f(\omega - \omega_1) = \delta(\omega - \omega_1) \quad (20)$$

In this case calculations are based on a single frequency, normally arranged so that $\omega_1 = \omega_0$ where ω_0 is the peak frequency of the absorption line.

Another possible laser shape function is an inverse Voigt profile

$$\begin{aligned} f(\omega - \omega_1) &= A \left[P\left(\frac{4}{5}, \frac{\omega - \omega_1}{\Delta\omega_1}\right) f_G(\omega - \omega_1) + Q\left(\frac{4}{5}, \frac{\omega - \omega_1}{\Delta\omega_1}\right) f_L(\omega - \omega_1) \right] \\ & \quad (21) \end{aligned}$$

Where $P(a,x)$ and $Q(a,x)$ are incomplete gamma functions, A is a normalisation constant and $\Delta\omega_1$ is the laser line width. A complete description of this function is given in the ESI.† The inverse Voigt function was used in the calculations of saturation power presented below.

Saturation is approached asymptotically with power and so a formal definition of the power required to produce saturation is required. Saturation intensity can be defined in terms of the laser gain coefficient $\gamma(\omega)$ (equivalent to a negative value absorption coefficient), Assuming $\gamma_0(\omega)$ is the small signal

($I = 0$) gain/absorption coefficient, generally, for a two-level atomic system:

$$\gamma(\omega) = \frac{\gamma_0(\omega)}{1 + \frac{I}{I_s(\omega)}} \quad (22)$$

When $\frac{\gamma(\omega)}{\gamma_0(\omega)} = \frac{1}{2}$, the intensity $I(\omega) = I_s(\omega)$ is called the saturation intensity. It can be shown that:

$$\frac{1}{I_s(\omega_1)} = \left(1 + \frac{g_k}{g_i}\right) \tau \frac{1}{c} g(\omega_1 - \omega_0) B_{ki} \quad (23)$$

Where g_k and g_i are the statistical weights of the upper and lower levels, respectively,

ω_0 is the frequency at the line centre and ω_1 the laser frequency,

B_{ki} is the transition probability for stimulated emission, and τ is the lifetime of the excited state.

The fluorescence output can be calculated for 2 cases, the small signal case when the population of the excited state is close to zero $N_k \approx 0$ or the large signal case close to saturation $N_k \rightarrow N_i$ which is most relevant here. Under these conditions, the fluorescence rate R is given by:

$$R = \frac{N_k}{N_i + N_k} A_{ki} \quad (24)$$

At saturation $I_s(\omega)/I_s(\omega) \gg 1$ so from eqn (22) $R \rightarrow R_s$. It can be shown that R_s reduces to:

$$R = R_s = \frac{g_k A_{ki}}{g_i + g_k} \quad (25)$$

Eqn (24) can be expressed in terms of $I_s(\omega)$ the saturation intensity (see for example She *et al.*⁵²).

$$R = R_s \left(\frac{I}{I_s(\omega_1)} \right) \frac{1}{1 + \left(\frac{I}{I_s(\omega_1)} \right)} \quad (26)$$

Table 2 presents data based on the above for both normal fluorescence (low signal case) and saturation for selected isotopes, but including the effects of using an inverse Voigt function for the laser line shape. A full description of the theory is given in the ESI.† Generally a transition probability of $> 10^7 \text{ s}^{-1}$ is required for CLS detection to be efficient.

Analytical performance of ICP-MS-CLS

The ion signal at a mass m is given by:

$$I_m^{\text{obs}} = S_m \times A_m \times C \times \eta \quad (27)$$

Where S is the instrumental sensitivity, A_m is the abundance of the isotope, C is the elemental concentration, and η the degree of ionisation.

The sensitivity in turn can be represented as the product of four terms:

$$S_m = Q \times \phi \times \varphi \times \theta \quad (28)$$

where

Q is the sample uptake rate,

ϕ is the efficiency of the sample introduction system in introducing analyte into the plasma,

ϕ is the mass spectrometric instrument transfer efficiency, reflecting the fraction of ions entering the plasma that reach the detector.

θ is the detection efficiency of the CLS detector.

Q —The sample uptake rate

For the kind of samples to which ICP-MS-CLS might be applied, the sample is likely to be scarce and so a micro-nebuliser operating in the 30–100 $\mu\text{l min}^{-1}$ range is likely to be the preferred sample introduction device.

ϕ —Efficiency of the sample introduction system

Micro-nebulisers typically achieve efficiencies of about 30%, but this can be raised towards 100% if a heater and desolvation system are employed.

ϕ —The mass spectrometric instrument transfer efficiency

Modern sector field instruments achieve sensitivities of the order of 3×10^9 cps per ppm for heavy elements with standard sample introduction systems running at about 1–2% efficiency.⁵³ For ^{238}Pu with a 1 ml per minute uptake rate this represents an overall transfer efficiency of 0.007%. Using a high efficiency sample introduction system involving a heated spray chamber and desolvation system, the sample introduction efficiency can be $\sim 100\%$ in which case the overall transfer efficiency can approach 0.1% (which is used in the calculations below).

Most of the losses in ICP-MS instrumentation occur in the ion extraction stage, particularly on the skimmer cone, and improvement in this area would be a major advance for both conventional ICP-MS and ICP-MS-CLS.

θ —The detection efficiency of the CLS detector

This includes contributions from:

- ion energy spread in determining the efficiency of optical pumping,
- uncertainty concerning the lower energy state of the ions,
- optical trapping and branching ratios, reflecting how many scattered photons are available for detection,
- the effect of hyperfine splitting,
- the optical collection efficiency,
- the quantum efficiency of the optical detector,
- the efficiency of the ion detector ($\sim 100\%$ for 5–10 keV ions),
- the effect of spurious BG counts from stray light photons and non-specific background ions,
- the combined abundance sensitivity reflecting the rejection of major isotopes at adjacent masses.

It is assumed here that the detection limit corresponds to a SNR of 3 and the N_s values shown in Table 14 are the signal counts required to yield this SNR for the various scenarios. Above about 10^4 cps, flicker noise dominates (see for example⁵⁴), but at the low levels most relevant to ICP-MS-CLS, only Poisson noise need be considered and hence SNR can be estimated from:

$$\text{SNR} = \frac{N_s}{(N_s + 2N_B)^{1/2}} \quad (29)$$

where N_s is the total signal count recorded and N_B the total BG count.

The CLS BG reduction factor is taken as an estimate from the simulation data provided in Table 1.

Two other important assumptions are made:

- that the ion energy problem has been resolved so that all the ions are sampled by the laser beam, *i.e.* pumping efficiency is unity,
- that all the ions enter the optical detector in their ground state.

The hyperfine factor is an approximation and is the reciprocal of half the number of available transitions (a justification for this estimate may be found above).

For a given branching ratio of α , $(1 - \alpha)$ represents the fraction of photons emitted at the resonant wavelength. As can be seen in Table 3, branching nevertheless usually produces a detectable photon (thus the branching factor is not specifically included in the calculation of detection limit), but its impact is felt in the consequential optical trapping that prevents re-pumping of the ion to produce a photon burst. In this case the optical efficiency has to be accounted for in the overall calculation, whereas for photon bursts, one trigger photon can nearly always be detected.

The following formula would provide an estimate of the combined effects of branching and optical efficiency, but it is too pessimistic and the actual calculation is as described above:

$$\text{Weighting} = ((1 - \alpha) + \alpha(\text{optical efficiency})) \quad (30)$$

Thus, if $\alpha = 0$, *i.e.* no branching occurs, the optical efficiency does not degrade the detection limit as at least one photon will be detected. However, if $\alpha = 1$, the full effect of the optical detection efficiency is reflected in the detection limit.

The data in Table 14 refer to the numbers of ions detected in a 10 minute run, unless otherwise stated, and these can be converted back to concentrations using the volume of sample processed (here expected to be 1 ml) and the relative atomic mass (a more detailed account of how the data in Table 14 were calculated is given in ESI†). Note that with typical instrumental BG's being of the order of 0.3 cps, a 10 minute count yields 180 counts (noise 13 counts). This would be reduced to $10^{-4} \times 0.108 \sim 0.02$ with CLS detection, indicating that, if required, much longer count times could be used to improve S/N. The data presented are for CLS mode detection which as explained above would not necessarily be the preferred option in all cases. Further, the parameters used have been selected to represent a worst case scenario and so a practical instrument should be able to deliver numbers of this order.

In the ideal, but unachievable, case of zero BG, with 0.1% transfer efficiency from beaker to ion counter, it should be possible to detect of the order of 10^4 ions (varying depending on the ionisation efficiency). Under zero BG conditions, CLS detection offers no benefits.

With zero BG and Poisson counting statistics the time of acquisition is immaterial, only the total number of counts, 9 in this case, is important. In the real situation, where background is always present, the time of acquisition does matter and

Table 14 (A) Estimated detection limits: assumed parameters, (B) estimated detection limits: calculated parameters and (C) estimated detection limits for selected isotopes

Parameter	Value
ϕ Efficiency of the sample introduction system (%)	100
ϕ The mass spectrometric instrument transfer efficiency (%)	0.1
MS abundance sensitivity	1×10^{-5}
Efficiency of ion counter (%)	100
Photon detector efficiency (%)	70
Random photon BG (cps)	30
CLS BG reduction factor	1000
Signal-to-noise ratio at DL	0.0004
BG counts (cps)	3
Signal at adjacent ($M \pm 1$) mass for same element (cps)	1×10^6
Run time for accumulation of BG counts	1×10^{10}
	10 min

(B) Estimated detection limits: calculated parameters						
Isotope	Mass	% Ionized	Branching ratio	Hyperfine factor	Optical abundance sensitivity	
$^{55}\text{Fe}^+$	54.938298	94.44	0.284	0.2	3.24×10^{-5}	
$^{63}\text{Ni}^a$ atom	62.929673	93.86	0.5	0.67	3.00×10^{-5}	
$^{90}\text{Sr}^+$	89.907738	99.89	0	1	5.66×10^{-6}	
$^{99}\text{Tc}^+$	98.906254	97.90	0.239	0.13	6.69×10^{-6}	
$^{147}\text{Pm}^+$	146.915134	99.78	0.82	0.13	1.13×10^{-7}	
$^{238}\text{U}^+$	238.050784	99.40	0.5	1	1.26×10^{-9}	
$^{238}\text{Pu}^+{}^b$	238.049553	99.82	0.00239	1	1.67×10^{-9}	
$^{241}\text{Am}^+{}^a$	241.056823	99.71	0.5	0.13	1.24×10^{-9}	

(C) Estimated detection limits for selected isotopes							
(i) Expressed as numbers of atoms							
Isotope	ICP-MS DL with no BG $N_S = 9$	ICP-MS DL with BG $N_S = 103979$	ICP-MS DL with M + 1 isotope $N_S = 32868$	ICP-MS DL with BG and M + 1 isotope $N_S = 109049$	ICP-MS-CLS DL with no BG $N_S = 9$	ICP-MS-CLS DL with M + 1 isotope of the same element Signal counts for SNR = 3 N_S	ICP-MS-CLS DL with BG and M + 1 isotope of the same element Signal counts for SNR = 3 N_S
$^{55}\text{Fe}^+$	9.54×10^3	1.10×10^8	3.48×10^7	1.16×10^8	2.27×10^5	192	5.26×10^7
^{63}Ni atom	9.60×10^3	1.11×10^8	3.51×10^7	1.16×10^8	6.82×10^4	185	1.58×10^7
$^{90}\text{Sr}^+$	9.02×10^3	1.04×10^8	3.29×10^7	1.09×10^8	9.02×10^3	83	2.09×10^6
$^{99}\text{Tc}^+$	9.20×10^3	1.06×10^8	3.36×10^7	1.11×10^8	3.37×10^5	90	7.80×10^6
$^{147}\text{Pm}^+$	9.03×10^3	1.04×10^8	3.30×10^7	1.09×10^8	3.31×10^5	16	7.66×10^7
$^{238}\text{U}^+$	9.06×10^3	1.05×10^8	3.31×10^7	1.10×10^8	4.32×10^4	9	9.99×10^6
$^{238}\text{Pu}^+$	9.03×10^3	1.04×10^8	3.30×10^7	1.09×10^8	9.03×10^3	9	2.09×10^6
$^{241}\text{Am}^+$	9.04×10^3	1.04×10^8	3.30×10^7	1.09×10^8	3.31×10^5	9	7.66×10^7

(ii) Expressed in relative units (for comparison) based on 10^4 atoms detected and a total of 1 ml of sample aspirated over a 10 minute period						
Isotope	$^{55}\text{Fe}^+$	^{63}Ni atom	$^{90}\text{Sr}^+$	$^{99}\text{Tc}^+$	$^{147}\text{Pm}^+$	$^{238}\text{Pu}^+$
Mass	54.938	62.93	89.908	98.906	146.915	238.05
Detection limit (g ml^{-1})	9.1×10^{-19}	1.0×10^{-18}	1.5×10^{-18}	1.6×10^{-18}	2.4×10^{-18}	4.0×10^{-18}

^a Indicates an estimated branching ratio of 0.5 and/or optical abundance sensitivity ^b Branching for Pu is small and therefore a photon burst is probable leading to unit optical detection efficiency.

hence a 10 minute acquisition period has been specified. This is longer than would normally be used in ICP-MS, but is well within the capabilities of CLS detection.

Introducing a BG at the analyte mass of 10^6 cps from an interfering ion, or from a major ion at $m/z \pm 1$ (in this case this could be from the same element, a different element or a molecular ion) which is present because of finite mass abundance sensitivity, raises the normal ICP-MS N_s by a factor of 10^4 to 103 979 counts which translates directly to a DL of about 10^8 ions. Apart from ions from isotopes of the same element (see below for this special case), these background ions are invisible to the photon detector, but can add counts to the CLS channel through adventitious correlations between the random photon BG and ions arriving at the ion detector. Taking a worst case scenario in which the random photon BG is 10^3 cps (restricting the laser power to 2 mW would reduce this to about 100 cps) and considering ions such as $^{10}\text{Be}^+$ and $^{90}\text{Sr}^+$ that produce photon bursts and have no fine structure, the CLS channel is 100% efficient and reduces the observed BG by at least a factor of 10^4 so N_s falls to $\sim 2 \times 10^3$ cps and DL's reduce by ~ 100 fold. In fact for these ions it would be possible to reduce the optical detection window length and improve the BG rejection factor further provided at least 5 photons can be acquired to overcome the optical detection efficiency. Thus, in the ideal case ICP-MS-CLS can reduce the detrimental effects of BG on DL's by 2–3 orders of magnitude. However, it must be pointed out that at 10^6 cps the linearity of the ion detector is within a factor of 2–3 of being into the pulse pile up region, so whilst there is the possibility of detecting this many ions, the dynamic range is < 10 . Analogue detection (dual mode multiplier or Faraday cup) is a possibility for normal mode MS, but nor for CLS. The same issue affects the introduction of an ion buncher, because whilst this would introduce multiplicity into the photon detection scheme and reduce BG even further, bunching effectively raises the instantaneous count rate and might move it into the pulse pile-up region where counts would be lost. Where appropriate, using optical detection alone avoids this difficulty.

The gain in performance is much less, a factor of 2–5, for odd numbered ions because optical trapping brings the optical detection efficiency into the equation and also the effects of hyperfine structure have to be taken into account. Carrying out the spectroscopy in a collision cell, or use of a two-colour pumping scheme as used in RIMS, would potentially overcome the trapping problem (see further comment in the Conclusions).

Thus, ICP-MS-CLS with current technology detectors is essentially an ultra-trace technique which extends the dynamic range of ICP-MS to lower DL's in the presence of spectral interference.

The next case considered is the presence of an isotope of the same element at an adjacent mass, *e.g.* ^{56}Fe adjacent to ^{55}Fe . A very high count rate of 10^{10} cps has been used which is of the same order as the strongest signals encountered in the ICP-MS spectrum. Ions of the same element, but with different isotopic mass, contribute to the BG in two ways.

Firstly, these ions can in principle be pumped by the laser, but very inefficiently because the combined effect of isotope

shift and the differential Doppler shifts lead to an optical abundance sensitivity in the range 10^{-5} – 10^{-9} . The combined abundance sensitivity derived from mass and optical discrimination, 10^{-9} – 10^{-14} , means that for heavy ions, isotopes of the same element are virtually invisible to causal CLS detection and for the lighter ions the effect on N_s is limited to raising it by a factor of ~ 20 (N_s for $^{55}\text{Fe} = 192$).

Secondly, their arrival at the ion detector maybe counted in the CLS channel through adventitious correlation with the photon BG. This adventitious detection, however, is degraded by the CLS BG rejection factor of 4×10^{-4} , so the total discrimination against these ions is the combined mass abundance sensitivity, 10^{-5} , and CLS BG rejection factor, 4×10^{-4} , *i.e.* 4×10^{-9} . This is slightly higher than the lowest combined mass and optical abundance sensitivity, in fact it would yield $N_s = 2184$. Thus, isotopes of the same element are more likely to be detected through adventitious triggering of the CLS detector than causal triggering through pumping.

ICP-MS-CLS is effective at dealing with interference from $m/z \pm 1$ ions for the photon burst ions with improvements in DL of 1–2 orders of magnitude. Once again the benefits are much less for ions that undergo optical trapping and/or have hyperfine structure.

The data presented in Table 14 for the combined effects of isobaric and $M \pm 1$ interferences closely follow the trends discussed above.

Conclusions

This paper has presented calculations that demonstrate both the potential benefits and problems of using the technique of co-linear laser spectroscopy for detection of ions in ICP-MS. Notwithstanding the benefits of employing a highly specific mode of ion detection, it remains that the ICP-MS interface is the limiting factor in determining the DL of the technique both in terms of its transmission and as the source of undesirable ion energy spread.

ICP-MS-CLS is a powerful technique for BG reduction for even numbered ions that yield photon bursts thereby providing unit detection efficiency for the optical detector. Gains in DL of at least 2 orders of magnitude are possible and effective abundance sensitivities for adjacent isotopes of the same element are in the range 10^{-9} – 10^{-14} . This makes ICP-MS-CLS a competitor for RIMS and AMS for favourable isotopes. For such ions, or when ion-bunching can be used, it may be preferred to use optical detection alone without ion correlation to avoid limitations imposed by the linear range of the ion counter.

Ions undergoing optical trapping pose a particular problem because they are likely to emit only 1 photon within the optical detector so that the optical detection efficiency of about 0.2 has to be factored into the DL calculation. As indicated above, collisional quenching of ions to the ground state or two-colour pumping schemes might be ways to overcome this problem. However, collisional quenching causes line broadening and would reduce the optical abundance sensitivity and multi-colour schemes would add further to the cost and complexity of the instrumentation.

Odd numbered ions also pose problems due to the presence of hyperfine structure which splits the transition into fine structure components. There is no obvious way to overcome this problem unless a broad-band laser is used to simultaneously pump the whole manifold, but this would reduce the optical abundance sensitivity.

A major difficulty exposed by this analysis is the ion energy spread encountered in ICP-MS which is typically of the order of a few eV. The calculations show that this must be reduced to $\sim 0.1\text{--}0.5$ eV to enable efficient laser pumping. Collision cells offer cooling to the order of $0.1\text{--}0.2$ eV, but the rf drive necessary to contain the ions limits the cooling that can be achieved because the buffer gas in the cell will re-partition energy from the transverse modes of the cell to axial motion of the analyte ion. The origins of energy broadening in ICP-MS are not well understood and this is an area for future research if ICP-MS-CLS is to be implemented as a practical technique. Work has been carried out in this laboratory to ascertain whether a 3D ion trap, which is widely used in ion cooling experiments and has been previously coupled to ICP-MS,⁵⁵ could be used to cool ions prior to CLS detection. The results of this work will be reported in a subsequent publication.

The ICP-MS-CLS instrument is complex and depends on the availability of lasers that can be accurately tuned and are stable for long periods. Currently such lasers are very expensive, but eventually developments in diode lasers may make it possible to use plug in modules or arrays of laser diodes to considerably reduce the cost.

ICP-MS-CLS can, under ideal circumstances, approach the detection limits required for radiometric bio-assays, $\sim 10^6$ ion L^{-1} , but not in its current state of development for all the required isotopes. A combination of group separation/pre-concentration and ICP-MS-CLS does, however, appear to offer a technique worthy of further investigation.

References

- 1 A. Montaser, *Inductively Coupled Plasma Mass Spectrometry*, Wiley-VCH, New York, 1998.
- 2 S. D. Tanner, V. I. Baranov and D. R. Bandura, *Spectrochim. Acta, Part B*, 2002, **57**, 1361.
- 3 S. D. Tanner, C. S. Li, V. Vais, V. Baranov and D. Bandura, *Anal. Chem.*, 2004, **76**, 3042.
- 4 F. Vanhaecke, L. Balcaen, I. Deconinck, I. De Schrijver, C. M. Almeida and L. Moens, *J. Anal. At. Spectrom.*, 2003, **18**(9), 1060.
- 5 W. Kutschera, *Int. J. Mass Spectrom.*, 2005, **242**(2–3), 145.
- 6 O. J. Marsden, F. R. Livens, J. P. Day, L. K. Fifield and P. S. Goodall, *Analyst*, 2001, **126**(5), 633.
- 7 K. Wendt and N. Trautmann, *Int. J. Mass Spectrom.*, 2005, **242**(2–3), 161.
- 8 C. Geppert, P. Muller, K. Wendt, C. Schnabel, H. A. Synal, U. Herpers and S. Merchel, *Nucl. Instrum. Methods Phys. Res., Sect. B*, 2005, **229**(3–4), 519.
- 9 J. Billowes, University of Manchester, personal communication, 1999.
- 10 M. A. Dexter, *Thesis*, Loughborough University, 2003.
- 11 C. M. Lock and E. Dyer, *Rapid Commun. Mass Spectrom.*, 1999, **13**(5), 432.
- 12 A. Nieminen, Manipulation of Low-energy Radioactive Ion Beams with an RFQ Cooler; Application to Collinear Laser Spectroscopy, Thesis, University of Jyväskylä, Finland, 2002.
- 13 A. Nieminen, P. Campbell, J. Billowes, D. H. Forest, J. A. R. Griffith, J. Huikari, A. Jokinen, I. D. Moore, R. Moore, G. Tungate and J. Aysto, *Phys. Rev. Lett.*, 2002, **88**(9), art. no. 094801.
- 14 A. Nieminen, P. Campbell, J. Billowes, D. H. Forest, J. A. R. Griffith, J. Huikari, A. Jokinen, I. D. Moore, R. Moore, G. Tungate and J. Aysto, *Nucl. Instrum. Methods Phys. Res., Sect. B*, 2003, **204**, 563.
- 15 B. L. Sharp and P. C. Goodall, *US Pat.* US2004099802, 2004.
- 16 S. G. Cox, A. D. J. Critchley, I. R. McNab and F. E. Smith, *Meas. Sci. Technol.*, 1999, **10**, R101–R128.
- 17 J. Billowes and P. Campbell, *J. Phys. G: Nucl. Phys.*, 1995, **21**(6), 707.
- 18 Photek Ltd, 2006, accessed 25/07/06, <http://www.photek.co.uk>.
- 19 D. A. Eastham, P. M. Walker, J. R. H. Smith, J. A. R. Griffin, D. E. Evans, S. A. Wells, M. J. Fawcett and I. S. Grant, *J. Phys. G: Nucl. Phys.*, 1986, **12**, L205.
- 20 MasCom Analysengeräte Service GmbH, Private Communication, 2006.
- 21 W. M. J. Fairbank, *Nucl. Instrum. Methods Phys. Res.*, 1987, **B29**, 407.
- 22 R. D. LaBelle, C. S. Hansen, M. M. Mankowski and W. M. J. Fairbank, *Phys. Rev. A: At., Mol., Opt. Phys.*, 1996, **54**, 4461.
- 23 D. A. Lewis, J. F. Tonn, S. L. Kaufamna and G. W. Greenless, *Phys. Rev. A: At., Mol., Opt. Phys.*, 1979, **19**, 1580.
- 24 A. G. Martin, S. B. Dutta, W. F. Gogers and D. L. Clark, *J. Opt. Soc. Am. A*, 1987, **B4**, 405.
- 25 D. A. Eastham, P. M. Walker, J. R. H. Smith, J. A. R. Griffin, D. E. Evans, S. A. Wells, M. J. Fawcett and I. S. Grant, *Opt. Commun.*, 1986, **60**, 293.
- 26 R. Payling and P. Larkings, *Optical Emission Lines of the Elements*, John Wiley & Sons Ltd, England, 2000.
- 27 NIST, *Atomic Spectra Database*, 1999, accessed 27/06/2006, http://physics.nist.gov/cgi-bin/AtData/lines_form.
- 28 R. L. Kurucz, *Kurucz Atomic Line Database*, accessed 17/08/2007, <http://kurucz.harvard.edu>.
- 29 F. S. Tomkins and M. Fred, *J. Opt. Soc. Am. A*, 1949, **39**, 357.
- 30 R. P. Thorne, *Spectrochim. Acta*, 1956, **8**, 71.
- 31 M. Fred and F. S. Tomkins, *J. Opt. Soc. Am. A*, 1957, **47**, 1076.
- 32 L. Bovey, *Spectrochim. Acta*, 1958, **10**, 383.
- 33 J. R. McNally, Jr and P. M. Griffin, *J. Opt. Soc. Am. A*, 1959, **49**, 162.
- 34 C. Bauche-Arnoult, S. Gerstenkorn and J. Vergès, *J. Opt. Soc. Am. A*, 1973, **63**, 1199.
- 35 J. Blaise, M. Fred and R. G. Gutmacher, *The Atomic Spectrum of Plutonium*, Argonne National Lab., IL, USA, 1984.
- 36 J. Blaise, M. Fred and R. G. Gutmacher, *J. Opt. Soc. Am. B*, 1986, **3**, 403.
- 37 M. C. Edelson, E. L. DeKalb, R. K. Winge and V. A. Fassel, *Spectrochim. Acta, Part B*, 1986, **41**, 475.
- 38 J. Blaise and J.-F. Wyart, *Energy Levels and Atomic Spectra of Actinides*, Laboratoire Aimé Cotton CNRS, Orsay, France, Orsay, 1992.
- 39 S. N. Nahar, *Astron. Astrophys.*, 1995, **293**, 967.
- 40 R. D. Cowan, *Programs RCN MOD36/HF MOD8 /RCN2 (Mod 36) Computation of Atomic Radial Wavefunctions*, 1993, accessed 20/08/2006.
- 41 P. Quinet, P. Palmeri and E. Biemont, *J. Quant. Spectrosc. Radiat. Transfer*, 1999, **62**, 625.
- 42 R. D. Cowan, *LANL: Atomic structure package*, 2000, accessed, <http://plasma-gate.weizmann.ac.il/FSfAPP.html>.
- 43 F. A. Parpia, C. F. Fischer and I. P. Grant, *Comput. Phys. Commun.*, 1996, **94**, 249.
- 44 P. Jonsson, F. A. Parpia and C. F. Fischer, *Comput. Phys. Commun.*, 1996, **96**, 301.
- 45 P. Jonsson, X. He and C. F. Fischer, 2000, personal communication.
- 46 D. M. Benton, E. C. A. Cochrane and J. A. R. Griffin, *J. Phys. B*, 1997, **30**, 5359.
- 47 H. J. Khun, *Atomic Spectra*, Longman Group, London, 1969.
- 48 N. J. Stone, *Table of Nuclear Magnetic Dipole and Electric Quadrupole Moments, Atomic Data and Nuclear Data Tables.*, 2005, vol. 75, p. 90.
- 49 R. Otto, H. Huhnermann, J. Reader and J. F. Wyart, *J. Phys. B*, 1995, **28**(16), 3615.
- 50 I. Sobel'man, *Atomic Spectra and Radiative Transitions*, Springer Verlag, Berlin, 1979.
- 51 K. Heilig, *Spectrochim. Acta, Part B*, 1977, **32**, 1.
- 52 C. Y. She and J. R. Yu, *Appl. Opt.*, 1995, **34**, 1063.

-
- 53 F. Pointurier, N. Baglan and P. Hemet, *Appl. Radiat. Isot.*, 2004, **60**(2-4), 561–566.
- 54 C. P. Ingle, P. K. Appelblad, M. A. Dexter, E. J. Reid and B. L. Sharp, *J. Anal. At. Spectrom.*, 2001, **16**(9), 1076.
- 55 C. J. Barinaga and D. W. Koppenaal, *Rapid Commun. Mass Spectrom.*, 1994, **8**, 71–76.
- 56 *Tables de Constantes (Tables Internationales de Constantes)*, Paris, 1992.